China Geology 9 (2026) 152−174

China Geology

Journal homepage: http://chinageology.cgs.cn
https://www.sciencedirect.com/journal/china-geology

Ground motion, liquefaction and hazard analysis at the Palu site during the 2018 Indonesian great earthquake (M_w 7.5)

Lindung Zalbuin Mase[a,*], Weeradetch Tanapalungkorn[b], Suched Likitlersuang[b, c], Kyohei Ueda[d], Tetsuo Tobita[e]

[a] *Department of Civil Engineering, Faculty of Engineering, University of Bengkulu, Bengkulu* 38371, *Indonesia*
[b] *Centre of Excellence in Geotechnical and Geoenvironmental Engineering, Department of Civil Engineering, Faculty of Engineering, Chulalongkorn University, Bangkok* 10330, *Thailand*
[c] *GreenTech Nexus: Research Center for Sustainable Construction Innovation, Faculty of Engineering, Chulalongkorn University, Bangkok* 10330, *Thailand*
[d] *Disaster Prevention Research Institute, Kyoto University, Kyoto* 611-0011, *Japan*
[e] *Department of Civil, Environmental and Applied System Engineering, Faculty of Environmental and Urban Engineering, Kansai University, Osaka* 564-8680, *Japan*

ARTICLE INFO

Article history:
Received 13 May 2024
Received in revised form 6 September 2024
Accepted 14 September 2024
Available online 17 February 2025

Keywords:
Shallow earthquake (M_w 7.5)
Ground motion
Liquefaction
Spectral matching method
Seismic Hazard Assessment
Structure damage

ABSTRACT

The research findings on the ground motion and liquefaction potential analyses during the 2018 Great Indonesia Earthquake (M_w 7.5) are significant and crucial. The earthquake triggered soil-structure damage due to liquefaction. This study, which thoroughly investigated four sites at Palu, was conducted by performing a comprehensive ground motion parameter analysis. The ground motion characteristics were presented and justified, particularly for the most impacted direction. Ground motion predictions were analysed to define the spectral accelerations, and matching spectral accelerations were conducted to produce ground motions for each site. Non-linear seismic ground response analysis based on the hyperbolic model of pressure pressure-dependent was performed to investigate cyclic soil behaviour. The results revealed that ground motion is crucial in significant soil damage, and the earthquake energy could trigger deep liquefaction. As the most significant ground motion, the vertical ground motion is essential in determining deep liquefaction. The discussion on the impact of liquefaction based on the results of the numerical analysis is presented. Significant ground motion with a longer duration could have a substantial impact on deep liquefaction in the study area. These findings depict how the 2018 Indonesia Earthquake (M_w 7.5) triggered a mega-liquefaction in Palu City. The results could enhance the understanding of the importance of seismic hazard assessment. It is recommended that site investigation and soil improvement should be planned to counteract liquefaction damage before construction. This study also suggests conducting seismic hazard assessments for city development to minimise the potential disaster impact in the study area.

©2026 China Geology Editorial Office.

1. Introduction

The Indonesian Archipelago is an area of the world's Ring of Fire. This condition could put Indonesia in a region of very high seismic intensity (Irsyam M et al., 2020). The events of massive earthquakes indicate the high seismic intensity in Indonesia. Two main types of earthquakes typically trigger significant earthquakes in Indonesia. They are subduction earthquakes and shallow crustal earthquakes. Mase LZ et al. (2023) state that subduction earthquakes generally occur in Indonesia. In contrast, shallow crustal earthquakes generally occur due to the activity of active faults in the land. Large-scale occurrences like the 2004 M_w 9.2 Aceh Earthquake (Meltzner AJ et al., 2006), the 2006 M_w 6.3 Yogyakarta Earthquake (Mase LZ et al., 2021a), the 2007 M_w 8.6 Bengkulu-Mentawai Earthquake (Mase LZ, 2017), and the 2018 Great Indonesia Earthquake in Palu (Socquet A et al., 2019). The Indonesia Agency of Meteorology, Climatology, and Geophysics (2022) reports that an inland earthquake with a magnitude of M_w 5.9 occurred. It is known as the Cianjur-West Java Earthquake of 2022. This earthquake is identified as an active fault beside the Lembang Fault (Somantri AK et

First author: *E-mail address*: lmase@unib.ac.id (Lindung Zalbuin Mase).

* Corresponding author: *E-mail address*: lmase@unib.ac.id (Lindung Zalbuin Mase).

Literary editor: Xi-jie Chen
doi:10.31035/cg2024067
2096-5192/© 2026 China Geology Editorial Office.

Copyright © 2026 Editorial Office of China Geology. Publishing services by Elsevier B.V. on behalf of KeAi Communications Co. Ltd.
This is an open access article under the CC BY-NC-ND License (http://creativecommons.org/licenses/by-nc-nd/4.0/).

al., 2023) that could trigger a low to moderate earthquake. West Java and Jakarta (the capital city of Indonesia) could become the most impacted area due to the activity of these active faults.

On September 28th, 2018, a shallow crustal earthquake counted with a magnitude of M_w 7.5 and a focal depth of 16 km (Yolsal-Çevikbilen S and Taymaz T, 2019). This earthquake, a stark reminder of the devastating power of nature, was triggered by the activity of the Palu-Koro Fault (Liu C and Shen YL, 2021), mainly due to the fault interaction, which induced stress between faults and significantly controlled the earthquake and its seismic hazards. Palu, the capital of the Province of Central Sulawesi, was recorded as the most impacted area during the area.

Several studies have explained the coseismic deformation and its impact on Palu's 2018 Great Indonesia Earthquake. Goda K et al. (2019) mentioned that the earthquake resulted in significant subsidence and deformation in Palu City. Sedimentary soils and hills underwent large ground-shaking amplifications and coseismic landslides. Goda K et al. (2019) also suggested that the earthquake demonstrated that major strike-slip events can trigger deadly and damaging tsunamis, to which multiple source mechanisms can contribute. Lee SJ et al. (2019) explained that coseismic seabed deformation is predicted to be about 0.4 m, which cannot trigger a massive tsunami. However, the horizontal coseismic deformation was relatively large, with a movement of about 3.6 m along the trace. Ulrich T et al. (2019) stated that the primary tsunami source might have been seismically generated vertical displacements. According to them, an average vertical displacement of 1.5 m on the offshore fault segment within Palu Bay was a tsunami source. Simons W et al. (2022) also mentioned that coseismic deformation had triggered the tsunami after the earthquake in Palu. The significant movement on the complex bathymetry or topography could build up the seawater, resulting in a tsunami. Jaya A et al. (2019) also suggested that the earthquake produced about 160 km long surface rupture with a maximum displacement of 5.8 m. Wu DY et al. (2021) reported coseismic displacements along surface ruptures and observed a maximum coseismic offset of about 6.2 m. Wu DY et al. (2021) also mentioned that based on their observation, the location of the Palu-Koro Fault is within the Palu Basin. A study by Natawidjaja DH et al. (2021) mentioned that a sizeable normal dip-slip during the earthquake exhibited a vertical displacement of 5 m.

One of the catastrophes that resulted from the earthquake was a massive liquefaction found in several areas in the plateau of the Palu Area. Several studies conducted by Kusumawardani R et al. (2021), Jalil A et al. (2021), and Widodo LE et al. (2022) reported that liquefaction in Palu had resulted in a huge geotechnical and structural damage. The existence of thick sedimentary soils and a significant earthquake led to the significant impact of liquefaction (Goda K et al., 2019). Several intensive studies conducted by Kiyota T et al. (2020), Hazarika H et al. (2020), and Okamura M et al. (2020) reported significant flow-side evidence due to liquefaction in Balaroa, Petobo, Jono Oge and Sibalaya. Besides the flow-side liquefaction, cyclic mobility liquefaction during the earthquake also happened. However, the characteristics of ground motion in controlling liquefaction and liquefaction analysis during the 2018 Great Indonesia Earthquake in Palu are still rarely found. Therefore, our unique approach to liquefaction site response analysis, which is a novel contribution to the field, still needs to be performed.

This study aims to explain the ground motion interpretation, liquefaction damage during the 2018 Great Indonesia Earthquake in Palu, and the liquefaction potential analysis. The impact of liquefaction on the study area and the importance of seismic hazard assessment in construction planning and spatial development are discussed. Generally, the results of this study verify the role of ground motion and site conditions in causing deep liquefaction in Palu. Additionally, the study provides recommendations on the importance of liquefaction hazard assessment for spatial plan development.

2. Theoretical framework and methodology

2.1. Seismotectonic setting

Sulawesi Island is one of Indonesia's active tectonic regions (Katili JA, 1978). Patria A and Putra PS (2020) mentioned that this island is located at the triple conjunction of plate convergence (Fig. 1). The triple conjunction plates include the Pacific, Australian, and Eurasian(Hall R, 2019). Under this condition, there is a complex seismotectonic setting in this region. Several tectonic formations, such as the Minahasa Trench, Sangihe Thrust, and Tolo Through, are formed due to the tectonic activities in this area (Komura K and Sugimoto J, 2021). In addition, several active faults, such as Palu-Koro, Matano, Walanae, and Lawanopo, have also been identified on this island. Consequently, Sulawesi is frequently under earthquake threats with a magnitude greater than 4.5 and a minimum shallow focal depth of 30 km, mainly in central-northern Sulawesi (Patria A and Putra PS, 2020).

Watkinson IM and Hall R (2017) and Cipta A et al. (2017) mentioned that the Palu-Koro Fault system is essential. The Palu-Koro Fault System is a major active NNW-SSE trending left-lateral strike-slip fault zone on the island of Sulawesi in Indonesia (Bellier O et al. 2001). Socquet A et al. (2006) explained that the Palu-Koro fault is a significant boundary and accommodates the 42 mm/year relative motion between the Makassar and North Sulawesi Regions (Fig. 1). This fault is also connected to the Matano Fault in the southern part of the Island. Patria A and Putra PS (2020) revealed that both faults moved left-lateral slip from the east-west convergence. Palu-Koro is extended to the north and terminates at the western part of the North Sulawesi Subduction.

Patria A and Putra PS (2020) mentioned that seismic activity in the Palu-Koro Fault is indicated by several earthquakes that occurred. The fault activity is generally classified as strike-slip. Cipta A et al. (2017) suggested that

the fault is the most significant seismic risk in eastern Indonesia, and it is also possible to produce a massive earthquake. This prediction seems relevant to the big earthquake in Indonesia that occurred on September 28, 2018. The activity of the Palu-Koro Fault triggered the earthquake. The earthquake's epicentre is located in the northern part of Sulawesi Island, about 80 km from Palu, the capital city (Jaya A et al., 2019). The earthquake triggered a 4 m tsunami wave that significantly impacted the city (Gusman AR et al., 2019). The earthquake also resulted in a mega-liquefaction in Palu City (Jalil A et al., 2021). Cipta A et al. (2021) mentioned that the combination of high-peak ground acceleration at the sites and complex geological mention triggered a mega-liquefaction during the 2018 Great Indonesia Earthquake.

2.2. Geological condition

Yulianur A et al. (2020) mentioned that the Palu Plain basin is dominated by deposited alluvial materials, such as sands and clays (Fig. 2). Rock formations in this area are sedimentary, volcanic, plutonic, and metamorphic. In the study area, the Holocene formation is dominant. The formations formed during the Holocene ages could be categorised as sedimentary rocks. During the 2018 Great Indonesia Earthquake, liquefaction evidence was found in Palu's basin area, which was dominated by sedimented and

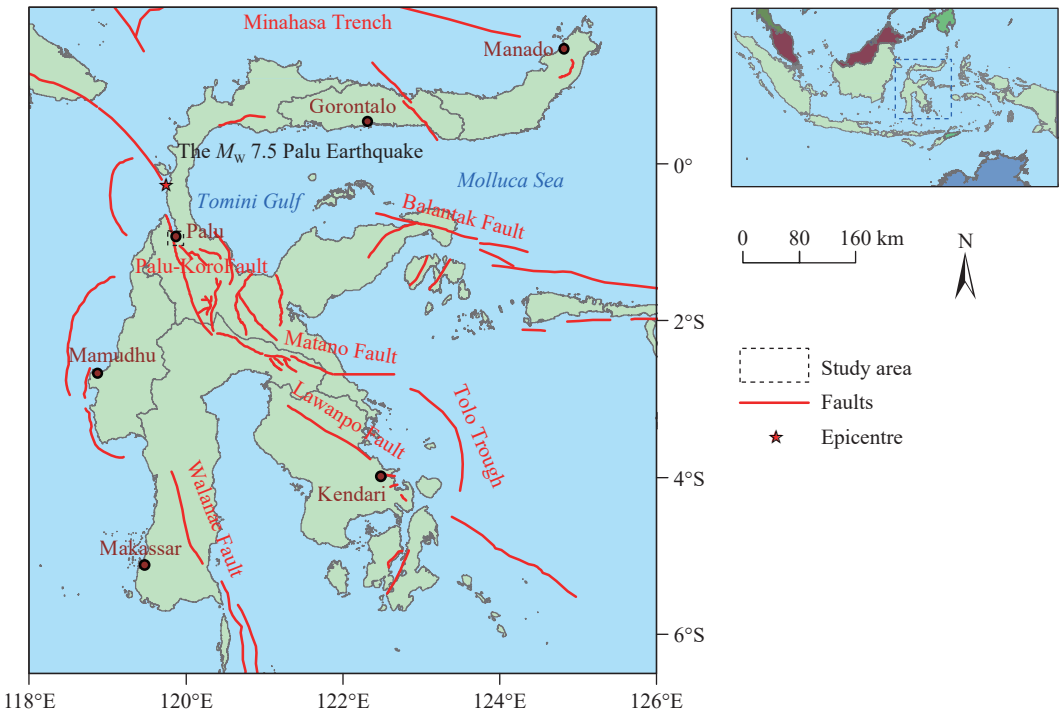

Fig. 1. Seismotectonic settings of the Palu study area.

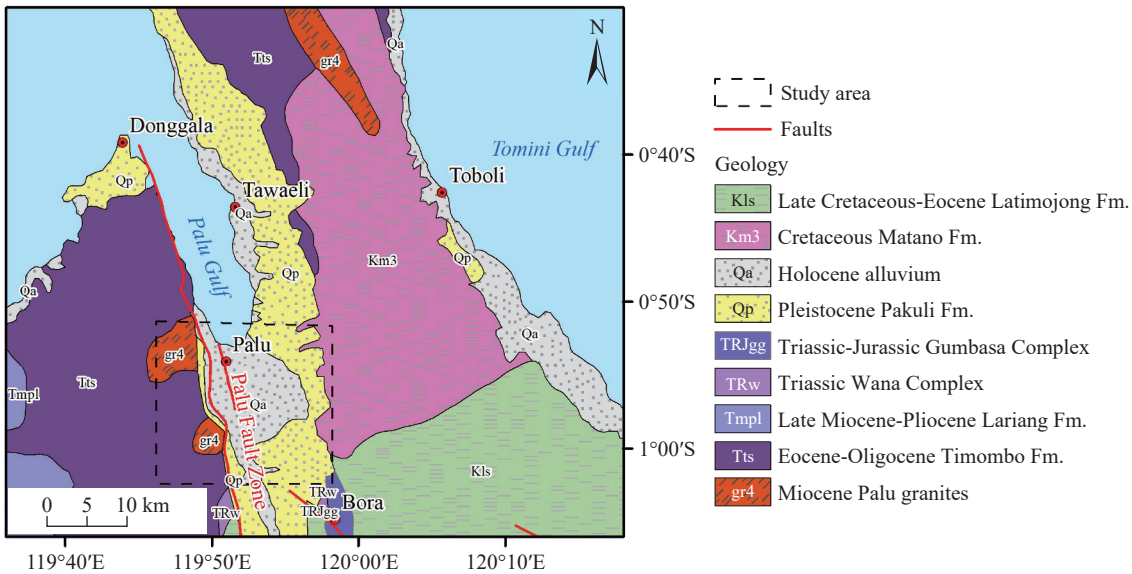

Fig. 2. Geological map of the Palu area.

Holocene sediment. Hibsch C et al. (1997) mentioned that liquefaction history could be found in sedimented materials, such as lacustrine sediment formed during Holocene. Munson PJ and Munson C (1995) mentioned that liquefaction in the past happened in sediment material during the Holocene ages. Holzer TL et al. (1999) suggested that the liquefaction potential for sedimented granular soil appeared more susceptible to liquefaction.

Fig. 3 shows the study area's geological situation and the study area's field survey map. Fig. 3 also shows that four locations were investigated in this study. These are called S-1 to S-4. P-1 is in Garuda, S-2 is in Pengau, S-3 is in Lere, and S-4 is in Dongala Kodi. The coordinates of the surveyed locations are summarised in Table 1. There is also a seismic station called the Seismic Station of Indonesian Meteorological, Climatology, and Geophysical Agency or locally, namely, PLS. This seismic station is located in Balaroa. In Fig. 3, the Palu-Koro Fault crosses Palu City. Therefore, the impact of the earthquake triggered by Palu-Koro is severe since this fault is crossing the settlement area (Walpersdorf A et al., 1998).

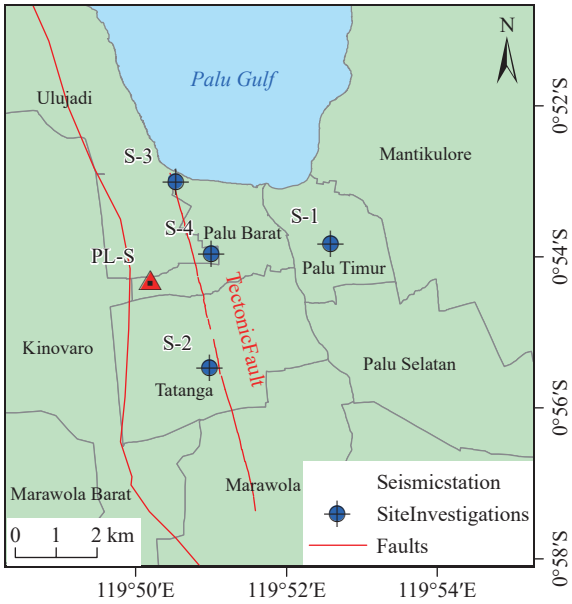

Fig. 3. Site investigation locations.

Soil and shear wave velocity profiles (V_s) are shown in Fig. 4. It should be noted that those parameters were estimated through geophysical measurements and were based on a previous study conducted by Thein P et al. (2014). In Fig. 4, it can be observed that sandy soils dominate the site condition in the study area. Those sandy soils are classified as silty sand (SM), clayey sand (SC), and gravelly sand (SG). Several clay layers dominated by silty clay (CM) are also found in the investigated sites. Field investigations show that the time-averaged shear wave velocity (V_{s30}) at the initial depth of 30 m varies between 201 m/s and 331 m/s. According to the National Earthquake Hazard Reduction Program (NEHRP, 2015, the study site should be categorised as site class D with a V_{s30} of 180–360 m/s. Wills CJ et al. (2015) and Hollender F et al. (2018) mentioned that V_{s30} is related to seismic vulnerability. The lower V_{s30} means an enormous potential for seismic vulnerability. Rusydi M et al. (2018) mentioned that at Palu Plain, the range of V_{s30} ranges from 200 to 300 m/s. Therefore, in line with NEHRP, the site class in Palu Plain is also categorised as Site Class D. Generally, the prediction made by Rusydi M et al. (2018) is consistent with this study. Fig. 3 shows that the study area's

Table 1. Locations of site investigation, epicentre, and seismic station.

Sites	Latitude	Longitude	Locations
S-1	0°53'49.45"S	119°52'35.09"E	Garuda
S-2	0°55'27.94"S	119°50'58.91"E	Pengawu
S-3	0°53'0.18"S	119°50'32.33"E	Lere
S-4	0°53'57.48"S	119°51'0.23"E	Donggala Kodi
M of 7.5	0°10'40.80"S	119°50'24.00"E	Epicentre
PL-S	0°54'18.51"S	119°50'11.86"E	Palu Seismic Station

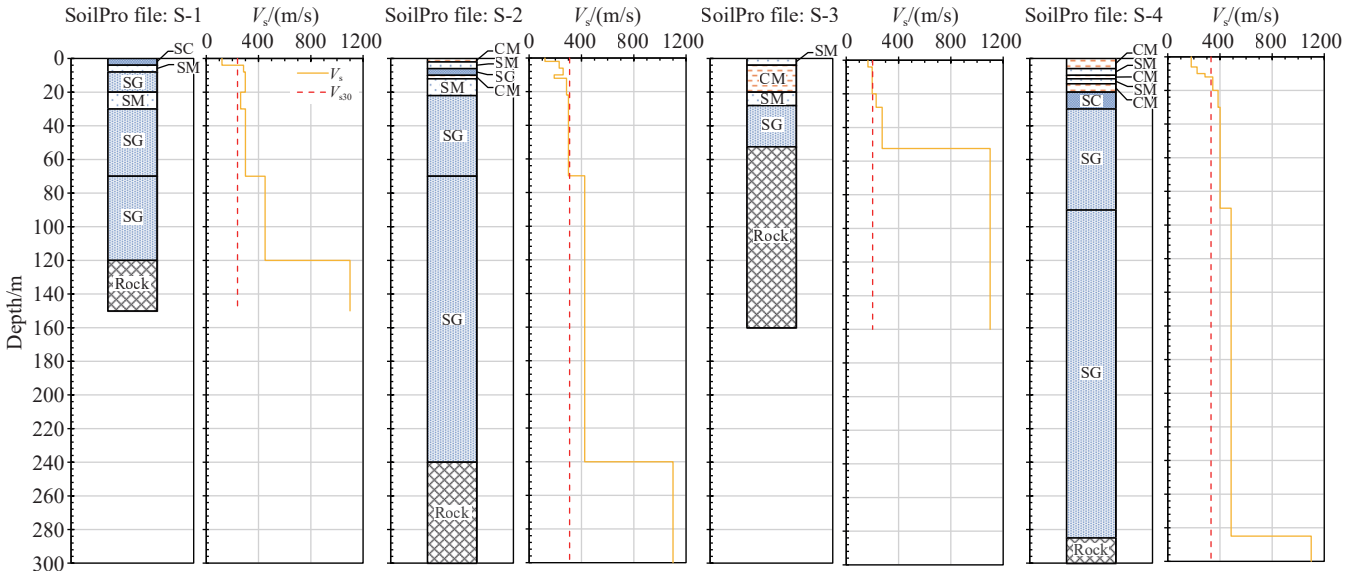

Fig. 4. Site investigation.

engineering bedrock depth varies from 52.5 m to 285 m below the ground surface. The prediction proposed by Rusydi M et al. (2018) also shows the depth of engineering bedrock in the study area from less than 25 m to more than 125 m. Rusydi M et al. (2018) also reported that shallow groundwater levels are also found in the central Palu Plain, which is consistent with this study.

2.3. Next-generation attenuation models and spectral matching analysis

Palu Seismic Station, or PLS Station, is the only seismic station that recorded the earthquake ground motion during the 2018 Great Indonesia Earthquake. The earthquake triggered the coseismic displacements along surface ruptures with a maximum coseismic offset of about 6.2 m. The significant impact of this earthquake is reflected by the ground motion record recorded in the PLS station. The recorded ground motion under baseline correction collected from PLS is presented in Fig. 5. In Figs. 5a–c, ground acceleration, ground velocity, and ground displacement of the earthquake are presented, respectively. It should be noted that velocity and displacement are derived based on differential techniques. From Fig. 5, it can be observed that there are three ground motions in three directions. For horizontal directions, east-west (EW) and north-south (NS), maximum peak ground accelerations (PGA_{max}) are 0.283 g and 0.205 g, respectively. For vertical direction or UD (up-down) direction, PGA_{max}) is 0.327g. In Fig. 5b, the velocity values for all directions (EW, NS, and UD) are 0.649 m/s, 0.763 m/s, and 0.758 m/s, respectively. According to Cilia MG et al. (2021), based on the Boore DM et al. (2014) model, the predicted PGV values for the liquefied site areas are about 0.6 m/s to 0.8 m/s. The prediction seems reasonable and consistent with the PGV values based on the PLS station. In Fig. 5c, based on the differential formulation from the time history of velocity, the displacement values for all directions (EW, NS, and UD) are 28.585 m, 29.326 m, and 42.719 m, respectively. The maximum PGD value is generally consistent with the resulting ground movement and displacement in several flow-side areas such as Balaroa, Sibalaya, Jono Oge, and Petobo during the earthquake, which are laterally moved up to several hundred meters.

Fig. 6 also shows the ground motion's spectral acceleration. Fig. 6 shows that the vertical direction's spectral acceleration exceeded the spectral acceleration design for stiff soils (SNI 1726-2019, 2019) at short periods. In contrast, spectral accelerations of the horizontal directions exceeded

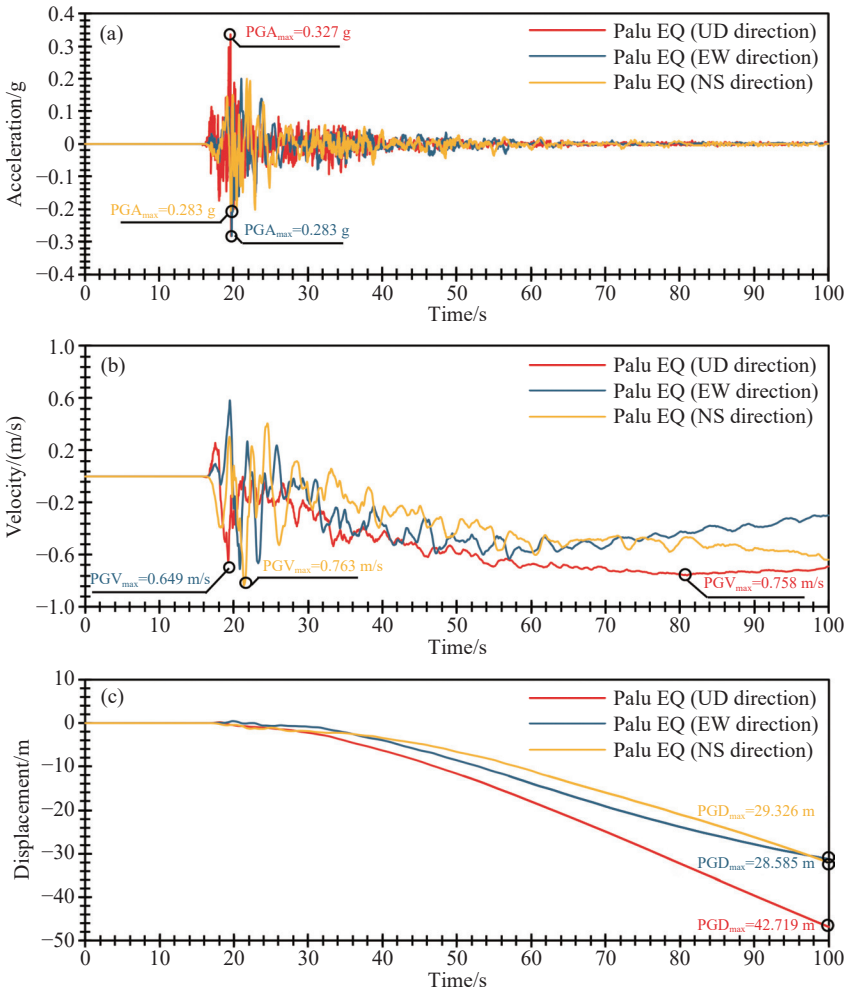

Fig. 5. Time-history of ground motion. a–Acceleration; b–velocity; c–displacement.

the design one for long periods. Generally, from the periods of 0.1 s to 1 s, it can be categorised as a critical condition. A period of 0.1 s could represent the low-story building period, and a period of 1s represents the high-story building period. Buildings that have periods close to the critical period range could undergo resonance effect. Therefore, it can make the damage more significant to soils and structures. Mase LZ et al. (2021b) also mentioned that the resonance effect resulted in massive damage to short to medium structures in Northern Thailand during the Tarlay Earthquake 2011.

In line with ground motion at the investigated sites, as presented in Fig. 3, four sites are investigated. The ground motion records did not exist at those sites because no seismic stations existed. Therefore, the prediction of ground motion should be performed. In this study, next-generation attenuation (NGA) model analysis is conducted. Abrahamson NA et al. (2014), Boore DM et al. (2014), Campbell KW and Bozorgnia Y (2014), Chiou BS and Youngs RR (2014), and Idriss IM (2014) are a few NGA-West2 models that could be used for research. Idriss IM (2014) model deals with rock sites. Within the study area, the explored sites are categorised as soil sites. In this manner, other models can be utilised to predict ground motion for the study area. NGA-West2 models were developed based on the uncertainty of earthquakes (Atik LA and Youngs RR, 2014). The parameters such as magnitude, rupture distance, site class, and fault mechanism determine ground motion prediction. Several cases of earthquake ground motion prediction, such as Tanapalungkorn W et al. (2020) in Northern Thailand, Abdulnaby W et al. (2020) in Iraq, and Huang C and Galasso C (2019) in China had shown the excellent performance of NGA-West2. NGA-West2 models forecast ground motion at the site, including peak and spectral ground acceleration. Moreover, the matched spectral acceleration is obtained by applying spectral matching and incorporated into the ground motion time history. This study employs the spectral matching

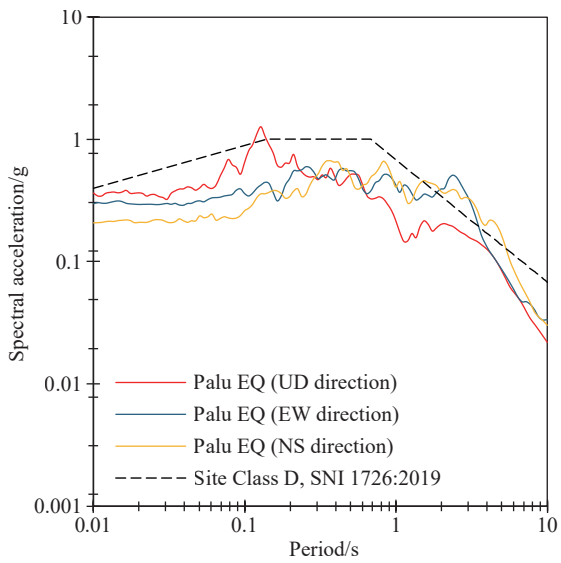

Fig. 6. Spectral acceleration of the M_w 7.5 Palu Earthquake recorded from the Palu seismic station (PL-S).

method proposed by Hancock J et al. (2006). The spectral matching method is initiated by determining the spectral acceleration from NGA-West2 models. After that, accelerograms can be adjusted by the spectral acceleration from the models to match a particular target response spectrum. This is done by applying the wavelets algorithm to produce a mean-matched spectrum whose maximum misfit corresponds to a predetermined tolerance. Next, the corresponding spectral acceleration is applied to the synthetic ground motion. This study uses the earthquake accelerogram from the PLS seismic station for the 2018 Great Indonesia Earthquake. The input for the seismic ground response analysis is the artificial ground motion. Considering the uncertainty of the studied earthquake, the generated ground motion is anticipated to represent the ground motion accurately. Therefore, the unavailable ground motions for studied sites may be resolved by applying the spectral matching method.

2.4. Summary of constitutive modelling

Several constitutive soil models, such as strain space multiple mechanisms and incremental plasticity model (Elgamal A et al., 2006), have been used to observe liquefaction behaviour during earthquakes under the framework of site response analysis. For example, by conducting an experimental test and a one-dimensional seismic ground response analysis, Mase LZ et al. (2019, 2022a) observed the liquefaction potential in the Izumio site in Osaka, Japan.

Non-linear soil behaviours are coupled using incremental plasticity and thus account for the hysteretic soil damping effect. The stress path and hysteretic load during cyclic mobility that soil could undergo during the dynamic load persisted in Fig. 7. Contractive sandy soils with low effective confining pressure (near surface) at initial stress at Point 0 could transform from contraction to dilation when shear loads are continuously performed. The transformation phase happens when the effective stress path achieves the phase transformation line (Point 1). The soil stiffness increment and effective stress path movement (Point 2). When the reverse load is applied, effective confining pressure reduction happens. Besides, sandy soil would behave as contractive material (Point 3 to Point 4). The excess pore pressure accumulation at Point 5 would follow this condition. Furthermore, it could fail at Point 6. The reverse of compression to the extension would reach the transformation line at Point 7. It will continuously result in shear strain and excess pore pressure accumulations (Point 8). With the same tendency to compression, it could fail at Point 9. The cyclic mobility phenomenon discussed by Ishihara K et al. (1975) inspired many researchers to develop constitutive modelling for liquefaction modelling.

Elgamal A et al. (2006) proposed a model to observe soil behaviour during earthquakes. This model incorporated the contractive, perfectly plastic, and dilative phases (Fig. 7) by

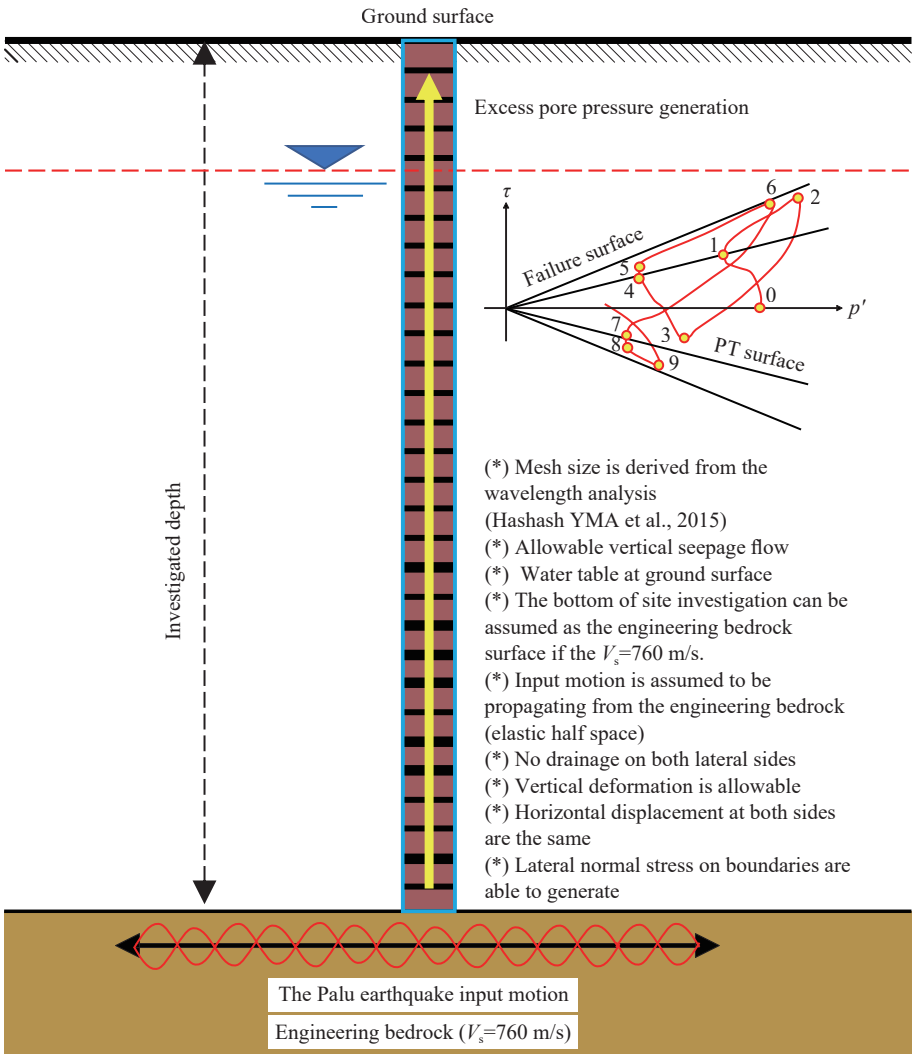

Fig. 7. Schematic model of 1D seismic ground response analysis.

developing a new appropriate flow rule. By incorporating a new flow rule, the model response characteristics are dramatically altered, recreating the prominent cyclic mobility processes and providing more direct control over the buildup of shear strain (based on experimental findings). A new hardening rule was also created for more reliable and effective numerical performance. The yield function (f) is selected based on Prevost JH (1985), as expressed in Eq. 1,

$$f = \frac{3}{2}(s-(p'+p'_0)\alpha):(s-(p'+p'_0)\alpha) - M^2(p'+p'_0)^2 = 0 \quad (1)$$

For the p more than 0 domain, $s = \sigma' - p'$; δ is the deviatoric stress tensor. σ'_0 is an effective Cauchy stress tensor, δ is a second-order identity tensor, and p' is mean effective stress, and p'_0 is a small post-light constant such that the yield surface size remains finite at p' (for numerical convenience and to avoid ambiguity in defining the yield surface normal at the yield surface apex. α is a second-order kinematic deviatoric tensor defining the yield surface coordinates. M dictates the yield surface size (defined by friction angle for the outmost surface). The pattern of ‘‘:’’ denotes a doubly contracted scalar product of two t contexts of multi-surface plasticity, several similar yield surfaces with a common apex and different sizes form the hardening zone.

The phenomena interplay between shear and volume change is handled by an appropriate non-associative flow rule inside the theory of plasticity framework. The present model restricts non-associativity to the volumetric component and makes the deviatoric component of the flow rule associative; by expressing P as the direction of plastic flow, the volumetric component P'' is defined as the desired degree of dilation or contraction according to experimental observations, as expressed in Eqs. 2, 3,

$$3P'' = \frac{1-(\eta/\bar{\eta})^2}{1+(\eta/\bar{\eta})^2}\psi \quad (2)$$

$$\eta = \frac{\sqrt{\frac{3}{2}s:s}}{p'+p'_0} \quad (3)$$

where η is the effective stress ratio, $\bar{\eta}$ is a material parameter defining the stress ratio for the transformation phase and ψ is a newly introduced scalar-valued function (Yang Z, 2000) to control contraction and dilation. It should be noted that if

$(1-(\eta/\bar{\eta})^2)$ is positive, the stress state lies within the transformation phase; if it is negative, it lies above the transformation phase.

Within the transformation phase surface (phase 0 to 1 in Fig. 7), contraction always occurs irrespective of loading or unloading conditions. The scalar-valued function (contraction) is expressed for state stress in the transformation phase.

$$\psi = c_1 \exp(c_2 p'/P_a) \tag{4}$$

where P_a is atmospheric pressure and c_1 and c_2 are two material constants governing the contraction rate (or, equivalently, the excess pore-pressure build-up rate under undrained circumstances). If confinement dependency is thought to be essential, parameter c_2 permits it. Parameter c_1 is dependent on the kind of soil and relative density.

On the phase of transformation surface (phases 1 to 2 in Fig. 7), Once an octahedral shear strain increment or γ_y accumulates, the stress state stays at D at low confinement levels close to liquefaction. This is caused by activating a constant volume in the perfectly plastic phase. The parameter offers significant versatility in controlling the near- and post-liquefaction yielding response magnitude. Specifically, the parameter γ_y is defined by

$$\gamma_y = y_1 + y_2 \gamma_T \tag{5}$$

$$\gamma_T = \int_0^t \gamma^P dt \tag{6}$$

where t is the time, and γ_T is the total octahedral plastic strain accumulated during liquefaction. The material constants are y_1 and y_2. Usually, loose soil requires a larger one. γ_2 can prolong the yielding phase y from one cycle to the next (the detail can be found in Chiarelli AS et al., 2003).

A dilatation tendency is activated for the above phase of transformation surface under loading and unloading conditions (phases 2 to 3 in Fig. 7). For loading condition, the formulation is expressed in the following,

$$\psi = d_1 \exp(d_2 \gamma_d) \tag{7}$$

where d_1 and d_2 are material constants, and d is cumulative octahedral plastic strain during the current dilative phase. Larger d_1 and d_2 values result in increasingly vital dilation, eventually limited by the conical yield surface gradient.

During the current dilative phase, d is the cumulative octahedral plastic strain, and d_1 and d_2 are the material constants. Larger d_1 and d_2 values produce more significant vital dilation, ultimately constrained by the conical yield surface gradient.

For unloading conditions (phases 3 to 4 in Fig. 7), a different definition of P'' is required to allow for a swift return to the confinement level p'_D upon unloading. To accommodate it, the relationship below is proposed,

$$\frac{\sqrt{3/2P' : P'}}{P''} = \frac{p'_D}{p'_R}\eta_f \tag{8}$$

where P' is the deviatoric component of the tensor P, η_f is the stress ratio along the failure surface, and p'_R is effective confinement at the load reversal. According to this rule, cumulative confinement is related to the contraction rate (Nemat-Nasser S and Tobita Y, 1982). The models of Dafalias YF and Manzari MT (1999) and Nemat-Nasser S and Zhang J (2002) also show that the contraction's reliance on prior dilation is consistent with experimental findings.

Using a purely deviatoric kinematic hardening rule (Prevost JH, 1985), the model efficiently produces a cyclic hysteretic response. Mróz Z (1967) mentioned that in the context of multi-surface plasticity, translation of the yield surface is generally governed by the consideration that no overlapping is allowed between yield surfaces. In this regard, Mróz Z (1967) proposed using the current (deviatoric) stress state (s) on the active surface for a new translation rule (μ), as expressed in the following,

$$\mu = \frac{M_{m+1}}{M_m}\left[s - \left(p' + p'_0\right)\alpha_m\right] - \left[s - \left(p' + p'_0\right)\alpha_{m+1}\right] \tag{9}$$

where $\left(p' + p'_0\right)\alpha_m$ and $\left(p' + p'_0\right)\alpha_{m+1}$ are the centres in the deviatoric plane. After updating the active surface, all inner surfaces are translated to be tangential at the updated stress state (s+ds) on the active surface. The translation rule of Eq. 9 was subsequently adopted by Dafalias YF and Popov EP (1975) in two-surface models and by Prevost JH (1985) in multi-surface model formulations.

Under specific loading conditions, it was discovered that Mroz's rule (Eq. 9) required a significant computational effort. This was especially noticeable at low confinement levels in the deviatoric plane, where yield surfaces have progressively smaller sizes. Therefore, in the model, a new translation rule (μ) was defined by Parra EJ (1996), as expressed in the following equation,

$$\mu = \left[s - \left(p' + p'_0\right)\alpha_m\right] - \frac{M_{m+1}}{M_m}\left[s - \left(p' + p'_0\right)\alpha_{m+1}\right] \tag{10}$$

where s_T is the deviatoric stress tensor. Eq. 10 is derived based on the Mróz Z (1967) conjugate points concept, allowing no yield surface overlap.

2.5. One-dimensional liquefaction site response analysis

This study performs a one-dimensional liquefaction site response analysis to investigate soil behaviour during the earthquake. It employs an open-source software called Cyclic1D (Elgamal A et al., 2006). The software is developed based on a finite element method framework for calculating one-dimensional seismic ground response subjected to lateral acceleration (Pender MJ et al., 2016).

The finite element formulation is a coupled solid-liquid approach that can simulate the generation and dissipation of excess pore water pressure. The cyclic mobility liquefaction pays attention to researchers that during cyclic loading, the stiffness could be changed. Elgamal A et al. (2006) adopted the principle of stiffness evaluation and followed the concept

of conical yield loci as suggested by Prevost JH et al. (1985). In this study, the illustration of the soil model employed in the analysis is derived based on Mase LZ et al. (2022a) in Fig. 7. It can be observed that the soil layer is divided into elements. The procedure to determine the size of the element is based on wavelength theory presented by Hashash YMA et al. (2015) as expressed by the Eq. 11,

$$d = \frac{V_s}{4 f_{\max}} \tag{11}$$

where, d is the mesh size and $f_{\max}$ is the maximum frequency. Hashash YMA et al. (2015) recommended that all layers should have the same frequency throughout the soil profile, and $f_{\max}$ should be generally a minimum of 30 Hz.

The input motion is applied to the engineering bedrock. The engineering bedrock is defined as a layer having a minimum V_s of about 760 m/s (Miller RD et al., 1999). Mase LZ et al. (2022b) mentioned that engineering bedrock could be considered the elastic half-space related to the application of input motion. The elastic half-space assumption is considered for ground motion applied as outcrop motion. Vertical seepage is allowed during excitation, whereas horizontal seepage is not allowed since there is no drainage path in the horizontal direction. This is because the excess pore pressure generation is generally generated upward. The excess pore pressure builds up to reduce effective stress. The liquefaction indication could be identified based on the comparison between effective stress and excess pore pressure, as expressed in the following,

$$\Delta u \geqslant \sigma'_v \tag{12}$$

where Δu is the excess pore pressure, and σ'_v is the effective stress. In Eq. 2, liquefaction could happen when the amount of Δu has the same value as σ'_v. From Eq. 12. Generally, the parameter called the excess pore pressure ratio could also be used as a liquefaction parameter,

$$r_u = \frac{\Delta u}{\sigma'_v} \tag{13}$$

where r_u is the excess pore pressure ratio. Liquefaction could happen when the excess pore pressure ratio exceeds one and vice versa.

During the liquefaction process, soil behaviours are presented, including the time history of excess pore pressure ratio, hysteresis loop, and effective stress path. Once the excess pore pressure exceeds the effective stress, it significantly reduces effective stress. It is also able to observe the effective stress path. Once the effective stress path becomes zero, liquefaction could happen.

2.6. Research framework

Fig. 8 presents the research framework of this study. This study is initiated by collecting data, such as site investigation data and earthquake ground motion records. This study's ground motion is the earthquake's ground motion with each direction component. The geological conditions and the seismotectonic settings in the study area are analysed.

The next step is to analyse the ground motion parameters from the recorded ground motion obtained from the closest seismic station to the studied area. Several ground motion parameters are presented: time-histories of acceleration, velocity, and displacement; energy flux; significant duration; and frequency content of ground motion (Kramer SL and Stewart JP, 1996). Those parameters are evaluated based on the direction component. The acceleration direction component is analysed at this step to determine the most significant acceleration. The justification for the most impacted ground motion is estimated based on the energy flux resulting from ground motion parameter analysis.

After the analysis, the most impacted ground motion and its direction are determined. The next step is to predict the maximum peak ground acceleration and spectral acceleration curve at observed sites. In this study, NGA models for soil sites are used. The spectral acceleration curve for each site is then determined, and the next step is to perform a spectral matching method (Hancock J et al., 2006) to determine ground motion. The most significant ground motion based on the ground motion parameter is then used as a matching spectral acceleration. Since the study area is categorised as a near-field zone (Mase LZ et al. 2022b), the recorded ground motion at the closest station could be used as a matching spectral acceleration to generate the ground motion for the study area.

Following the acquisition of ground motion data for every site under investigation, a one-dimensional seismic ground response analysis is carried out (Elgamal A et al., 2006). The information on site geotechnical properties is presented. Due to data limitations, several numerical analysis data are assumed, especially the dilative and contractive parameters. It should be noted that parameters including p'_{ref}, γ_{max}, Liq, c_1, c_2, d_1, and d_2 are determined based on recommendations suggested by Elgamal A et al. (2006). However, the assumptions are generated based on the geotechnical parameters available in this study. The input parameters used in this study are listed in Table 2. In this study, the framework of seismic ground response analysis suggested by Mase LZ (2017) and Mase LZ et al. (2022b) is adopted in the analysis. The V_s criterion of engineering bedrock based on Miller RD et al. (1999) is also implemented in seismic ground response analysis. Dynamic behaviour of soils, such as excess pore pressure ratio, hysteresis loops, and effective stress path, is presented. This study also compares the spectral acceleration design for the spectral acceleration of seismic ground response analysis.

3. Results and discussions

3.1. Ground motion parameters

Table 3 presents the ground motion parameters for all directions. Table 3 shows that acceleration in the UD direction or UD acceleration has the highest acceleration

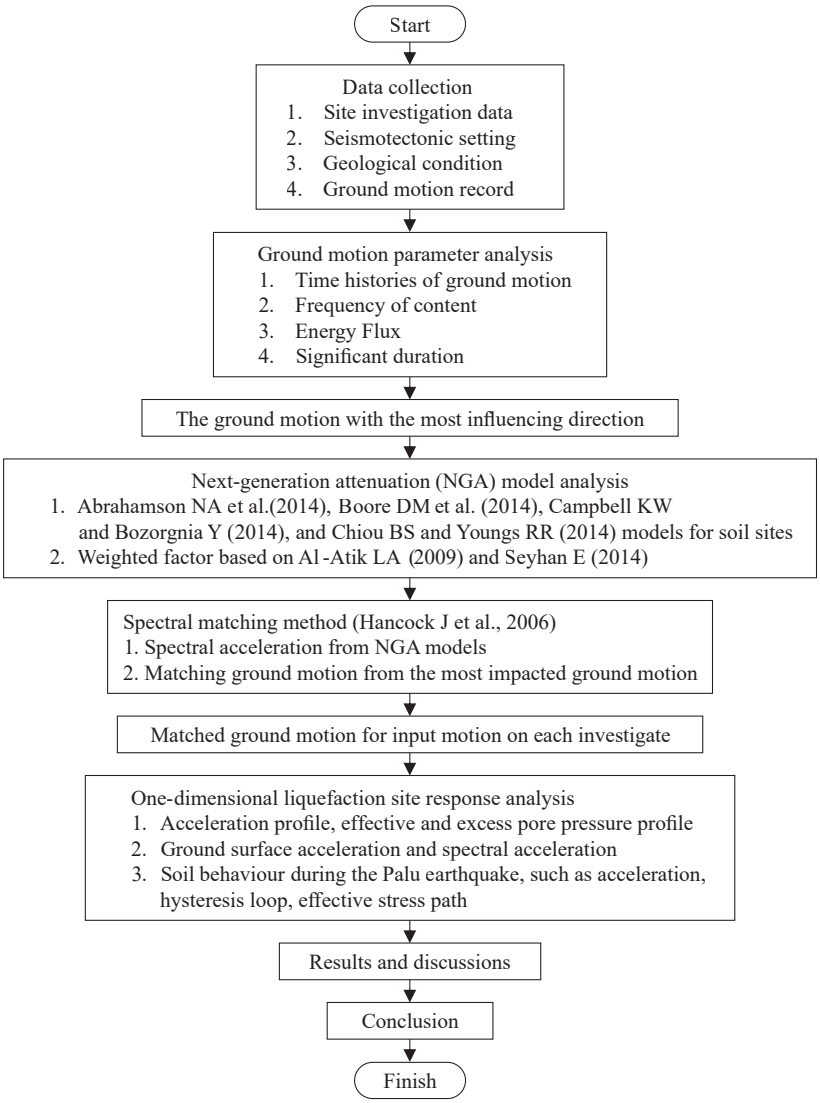

Fig. 8. Flowchart of the research framework.

value, i.e., 0.327g. Generally, the maximum acceleration occurred at 19.61 s. Both UD and NS velocities have a higher value compared to EW velocity. The maximum UD velocity generally occurred within 20 s to 81 s. In terms of maximum displacement, it is also observed that the maximum displacement obtained from the analysis is about 29.326 m to 42.719 m. Based on the analysis, the UD displacement results are the highest. Sarma SK and Yang KS (1987) suggested that the parameter of acceleration containing 95% AI or A95 could be used to assess how destructive the ground motion is. This study also shows that A95 for UD acceleration tends to have the highest. In addition, UD acceleration has the highest specific energy density among all accelerations.

Fig. 9 presents the intensity content for energy flux and arias intensity (AI) from the ground motions. Fig. 9a presents the energy flux of ground motions during the 2018 Great Indonesia Earthquake in 2018. It can be observed that the UD direction tends to result in the highest energy flux compared to the other two ground motions. Fig. 9b presents the Arias Intensity in Percent (%) and time (in seconds) corresponding to each ground motion. In Fig. 9b, the predicted significant duration can be estimated based on the time required to reach 5% Arias Intensity and 95% Arias Intensity. According to Fig. 9b, significant durations for each direction are 16.62 s (UD), 19.848 s (NS), and 21.406 s (EW), respectively. As a result, it is possible to calculate that the 2018 Great Indonesia Earthquake had an average significant duration of 19.291 s.

According to the analysis of ground motion parameters, the earthquake's UD direction is thought to have been a major contributing factor to the significant ground damage in the study area. As a result, the ground motion generated from the UD direction can be utilised as a representative ground motion for seismic ground response analysis for each site under investigation. The following section presents the findings of the spectral matching analysis for representative ground motion in each site under investigation.

3.2. Spectral matching results

During the 2018 Great Indonesia Earthquake, no actual ground motions were recorded in each investigated site. The only recorded ground motion was collected from the PL-S Station. The Next Generation Attenuation (NGA) models in

Table 2. Input parameters.

Sites	Layer Number	Soil Type	V_s/(m/s)	FC/%	Thickness/m	c/(kN/m^2)	φ/°	k/(m/s)	γ/(kN/m^3)	K_o	p'_{ref}/kPa	γ_{max}/%	Liq	c_1	c_2	d_1	d_2
S-1	1	SC	120	21	4	2.20	28	11.0×10^{-6}	16.81	0.53	80	5	0.03	0.30	0.20	0.00	10
	2	SM	285	8	4	2.15	19	66.0×10^{-6}	19.17	0.67	80	5	0.02	0.20	0.30	0.10	10
	3	SG	299	15	12	1.00	30	88.0×10^{-6}	18.75	0.50	80	5	0.02	0.20	0.30	0.15	10
	4	SM	263	9	10	2.50	21	66.0×10^{-6}	17.88	0.64	80	5	0.01	0.10	0.40	0.30	10
	5	SG	300	16	40	1.45	32	66.0×10^{-6}	17.87	0.47	80	5	0.01	0.10	0.50	0.40	10
	6	SG	450	16	50	1.54	33	66.0×10^{-6}	18.89	0.46	80	5	0.00	0.10	0.50	0.50	10
	7	Rock	1100	–	30	~	35	0.123×10^{-9}	22.34	0.43	80	5	0.00	0.01	0.59	0.60	10
S-2	1	CM	120	80	2	15.00	2	1.11×10^{-9}	17.30	0.97	50	5	–	–	–	–	–
	2	SM	229	8	4	2.37	19	66.0×10^{-6}	18.66	0.67	80	5	0.03	0.30	0.20	0.00	10
	3	SC	260	20	4	4.00	28	11.0×10^{-6}	18.64	0.53	80	5	0.02	0.20	0.30	0.10	10
	4	CM	192	82	2	16.00	2	1.11×10^{-9}	17.32	0.97	50	5	–	–	–	–	–
	5	SM	286	9	10	3.00	21	66.0×10^{-6}	18.46	0.64	80	5	0.02	0.10	0.30	0.15	10
	6	SG	300	15	48	2.32	32	88.0×10^{-6}	17.93	0.47	80	5	0.00	0.10	0.50	0.40	10
	7	SG	425	15	170	2.15	33	88.0×10^{-6}	17.82	0.46	80	5	0.00	0.10	0.50	0.50	10
	8	Rock	1100	–	60	~	35	0.123×10^{-9}	22.54	0.43	80	5	0.00	0.01	0.59	0.59	10
S-3	1	SM	166	9	4	3.13	19	66.0×10^{-6}	17.99	0.67	80	5	0.01	0.10	0.40	0.30	10
	2	CM	198	80	16	16.00	3	1.11×10^{-9}	17.37	0.95	50	5	–	–	–	–	–
	3	SM	228	10	8	3.21	19	66.0×10^{-6}	17.40	0.67	80	5	0.03	0.30	0.20	0.00	10
	4	SG	275	14	24.5	2.15	31	88.0×10^{-6}	17.71	0.48	80	5	0.00	0.10	0.50	0.40	10
	5	Rock	1100	–	108.3	~	35	0.123×10^{-9}	22.54	0.43	80	5	0.00	0.01	0.59	0.59	10
S-4	1	CM	180	83	6	17.00	3	1.11×10^{-9}	17.51	0.95	50	5	–	–	–	–	–
	2	SM	225	11	4	3.13	21	66.0×10^{-6}	18.60	0.64	80	5	0.01	0.10	0.40	0.30	10
	3	CM	285	81	2	16.00	4	1.11×10^{-9}	19.94	0.93	50	5	–	–	–	–	–
	4	SM	345	9	3	2.37	23	66.0×10^{-6}	20.35	0.61	80	5	0.02	0.10	0.30	0.15	10
	5	CM	345	80	5	15.00	3	1.11×10^{-9}	19.99	0.95	50	5	–	–	–	–	–
	6	SC	385	21	10	4.00	28	11.0×10^{-6}	19.90	0.53	80	5	0.02	0.20	0.30	0.10	10
	7	SG	401	15	60	2.32	32	88.0×10^{-6}	18.80	0.47	80	5	0.00	0.10	0.50	0.40	10
	8	SG	485	16	195	1.54	33	88.0×10^{-6}	18.66	0.46	80	5	0.00	0.10	0.50	0.50	10
	9	Rock	1100	–	15	~	35	0.123×10^{-9}	23.41	0.43	80	5	0.00	0.01	0.59	0.59	10

Note: γ and FC are unit weight and fine content, respectively; p'_{ref} is effective confinement pressure reference; c and φ are cohesion and internal friction angle, respectively; γ_{max} is peak shear strain; k is the permeability coefficient; Liq is the liquefaction parameter; V_s is shear wave velocity; c_1 and c_2 are contractive parameters; K_0 is the coefficient of lateral earth pressure at rest; d_1 and d_2 are dilative parameters

this study are employed to predict each investigated site's maximum and spectral acceleration. Only those four soil site models are used in this study because the area is classified as a soil site. Based on the weighted average of NGA-West2 models, the NGA-West2 is computed. The average spectral acceleration for each site is calculated to reduce the uncertainty of each model. Atik LA (2009) and Seyhan E (2014) presented the weighted factor for NGA models' calculation. For spectral matching analysis. This study uses spectral and time-history accelerations in the UD direction as the matching parameters.

Fig. 10 presents the site study's spectral acceleration prediction and spectral matching analysis. In Fig. 10, the red line indicates the spectral acceleration of NGA West2. Two red dashed lines also represent the standard deviation of NGA West2 spectral attenuation. The yellow line represents the spectral acceleration of recorded ground motion. Generally, based on NGA West2 prediction, the peak ground acceleration (PGA) for the study area is observed to vary from 0.366g to 0.547g. Scawthorn C (2018) mentioned that the MMI scale of IX to X indicated liquefaction, landslides, and shifted sand mud could occur. This description seems consistent with field evidence of the 2018 Great Indonesia Earthquake, as Faris F et al. (2019) reported.

Additionally, Fig. 10 demonstrates that each site under investigation's matched spectral acceleration is generally consistent with matching spectral acceleration. A similar method and its implementation have also been implemented by Mase LZ and Likitlersuang S (2021) to predict ground motion in Northern Thailand. Mase LZ et al. (2022a) mentioned that the method could effectively predict ground motion for sites near the seismic station. The matched spectral acceleration can generate the representative ground motion for each site. In Fig. 10, the comparison between matched spectral acceleration and recorded ground motion is generally consistent. The PGA from the spectral matching method varies from 0.447g to 0.532g for the investigated sites. Since the position of each investigated site is relatively close to the epicentre, the peak ground acceleration could be more significant. The generated ground motion is used as the input

Table 3. Ground motion parameters of the Palu Earthquake.

Parameter	Direction of Acceleration			Unit	Reference
	UD	EW	NS		
Maximum Acceleration (PGA_{max})	0.327	0.283	0.205	g	Kramer SL and Stewart JP (1996)
Time of PGA_{max}	19.61	19.759	19.637	s	Kramer SL and Stewart JP (1996)
Maximum Velocity (PGV_{max})	0.758	0.649	0.763	(m/s)	Kramer SL and Stewart JP (1996)
Time of PGV_{Max}	80.99	20.81	21.363	(s)	Kramer SL and Stewart JP (1996)
Maximum Displacement (PGD_{max})	42.719	28.585	29.326	(m)	Kramer SL and Stewart JP (1996)
Time of PGD_{Max}	99.98	99.998	99.998	(s)	Kramer SL and Stewart JP (1996)
V_{max}/A_{max}	0.216	0.234	0.379	(s)	Kramer SL and Stewart JP (1996)
Acceleration Root Mean Square (Acc_{RMS})	0.023	0.025	0.027	(g)	Kramer SL and Stewart JP (1996)
Velocity Root Mean Square (Vel_{RMS})	0.501	0.351	0.363	(m/s)	Kramer SL and Stewart JP (1996)
Displacement Root Mean Square ($Disp_{RMS}$)	19.96	1436.5	1306.919	(m)	Kramer SL and Stewart JP (1996)
Arias Intensity (AI)	0.808	0.988	1.126	(m/s)	Park YJ et al. (1985)
Characteristic Intensity (CI)	0.035	0.040	0.044	(Ic)	Cabañas L et al. (1997)
Specific Energy Density (SED)	25.089	12.305	13.187	(m^2/s)	Kramer SL and Stewart JP (1996)
Cumulative Absolute Velocity (CAV)	8.616	10.675	11.299	(m/s)	Cabañas L et al. (1997)
Acceleration Spectrum Intensity	0.232	0.200	0.197	(g·s)	Von Thun JL et al. (1988)
Velocity Spectrum Intensity (VSI)	1.087	1.873	1.908	(cm)	Von Thun JL et al. (1988)
Housner Intensity (HI)	107.409	202.983	201.79	(m)	Kramer SL and Stewart JP (1996)
Sustained Maximum Acceleration (SMA)	0.196	0.2	0.202	(g)	Nuttli OW et al. (1979)
Sustained Maximum Velocity (SMV)	0.684	0.577	0.555	(cm/s)	Nuttli OW et al. (1979)
Effective Design Acceleration (EDA)	0.305	0.277	0.203	(g)	Benjamin JR (1988)
Acceleration Containing 95% AI (A95)	0.323	0.279	0.202	(g)	Sarma SK and Yang KS (1987)
Predominant Period (T_0)	0.120	0.260	0.380	(s)	Kramer SL and Stewart JP (1996)

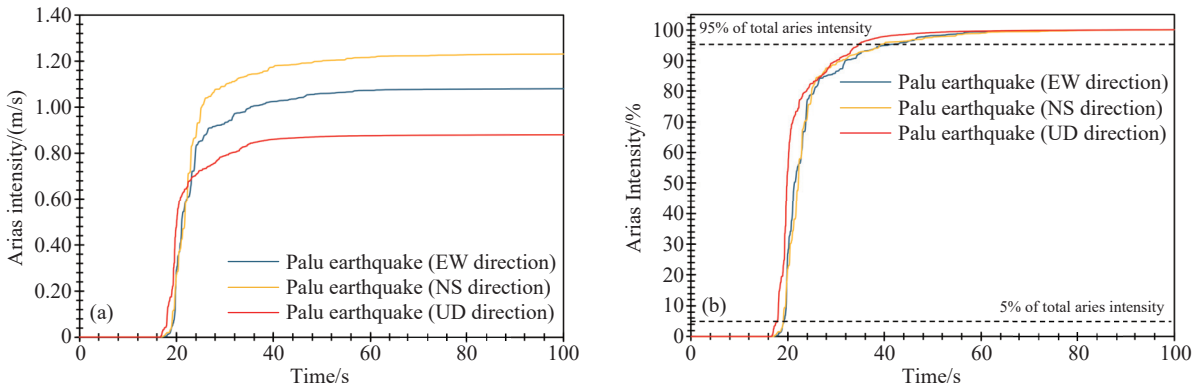

Fig. 9. Intensity content for a–Energy Flux and b–Arias Intensity.

motion for seismic ground response analysis, according to the results of the spectral matching analysis. Given that the uncertainty in the NGA model analysis was taken into account along with the actual ground motion record in the study area, the ground motions produced by this study may be pertinent to the sites.

Fig. 11 presents profiles of maximum accelerations, pressures, and settlement values during earthquake shaking for the investigated sites. Fig. 11a presents the results for S-1. As shown in Fig. 11a, the excess pore pressure exceeded the effective stress path for a relatively thick thickness. For S-1, it is predicted to be about 15 m (liquefied zone). The excess pore pressure is greater than the soil's effective stress in this zone. Evidence shows that the first three sand layers were liquefied during the 2018 Great Indonesia Earthquake. These sand layers are clayey sand (SC), silty sand (SM), and gravelly sand (SG). Fig. 11b presents the results for S-2. In S-2, the liquefaction during the 2018 Great Indonesia Earthquake is predicted to occur from 2 m to 10 m depth and 12 to 15 m depth. Layers indicated to undergo liquefaction are silty sand (SM) and clayey sand (SC). Fig. 11c presents the results for S-3. Similar to both previous sites, the liquefaction indication is also found in S-3, especially from 0 to 4 m and 20 m to 30 m. This depth range's excess pore pressure ratio exceeds the initial effective stress. In silty sand (SM), the liquefaction also takes place. Fig. 11d presents the results of the analysis for S-4. The liquefaction indication in this site is generally found at depths 6 m to 20 m. In Fig. 11d, the excess pore pressure exceeds the effective stress at this depth range. Similar to other investigated sites, sand layers classified as silty sand (SM) are relatively vulnerable to liquefaction in this site.

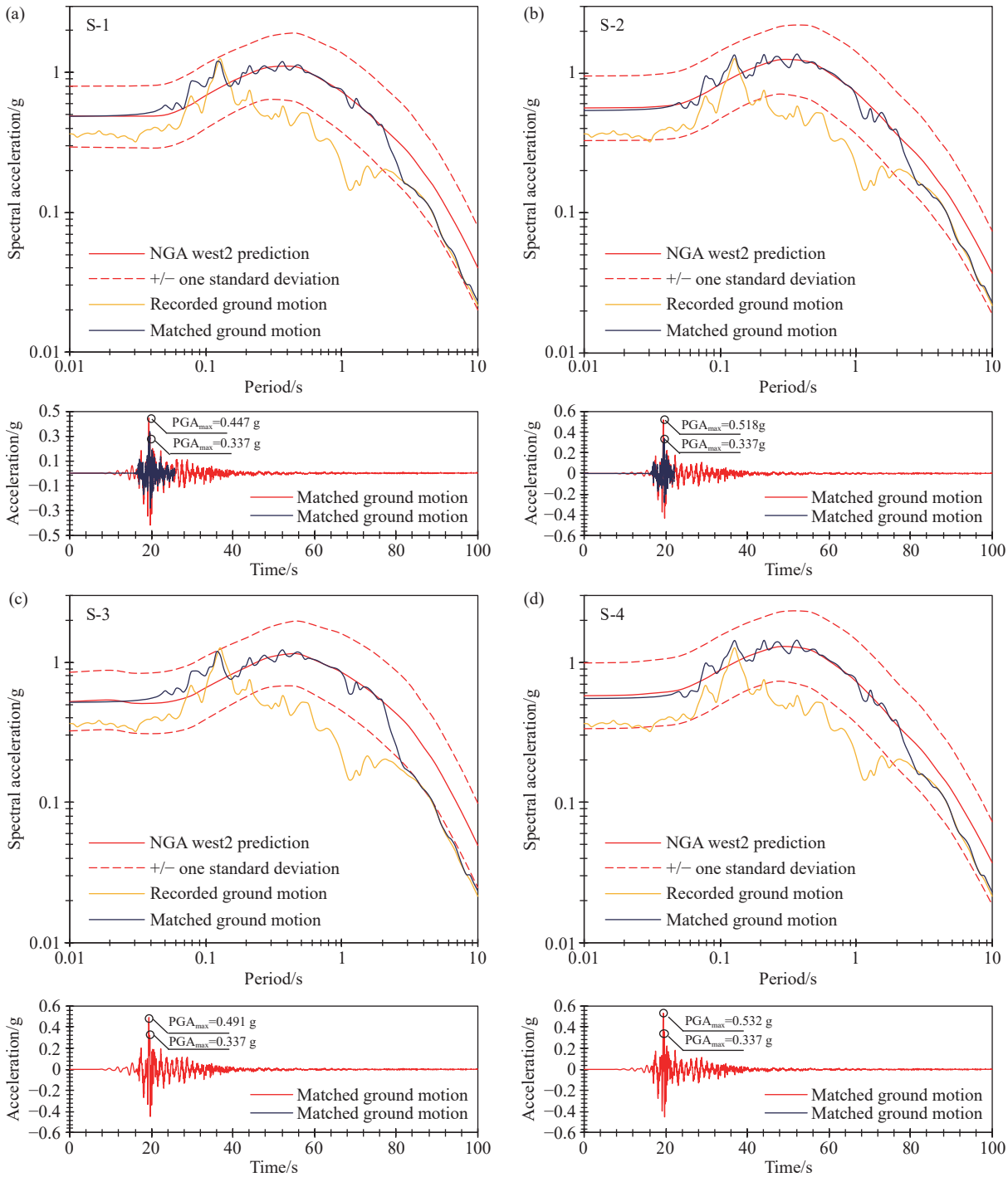

Fig. 10. Spectral matching results for a–S-1, b–S-2, c–S-3, and d–S-4.

3.3. Ground responses profiles

3.3.1. Pore pressure profiles

The uniform sand layer with low resistance and the large external force from the earthquake could be why liquefaction could happen massively in this area. This condition could be fulfilled if groundwater deposits and soil material permeability are available. It seems reasonable why liquefaction in a very thick sand layer could occur. The existence of uniform sand layers with low soil resistance could also be why massive liquefaction in a thick sand layer could occur in the study area. Significant liquefaction during the 2018 Great Indonesia Earthquake could occur due to the high permeability difference during pore water pressure dissipation in the liquefied layer, resulting in void redistribution in layers overlain by the low permeability layer. This void ratio increase triggered a significant shear strength loss in the corresponding layer (Tanjung MI et al., 2022). This effect can be worse if a strong earthquake with a vast magnitude of acceleration occurs (Santucci de Magistris F et al., 2013).

3.3.2. Acceleration profiles

For S-1 (Fig. 11a), the peak ground acceleration at the

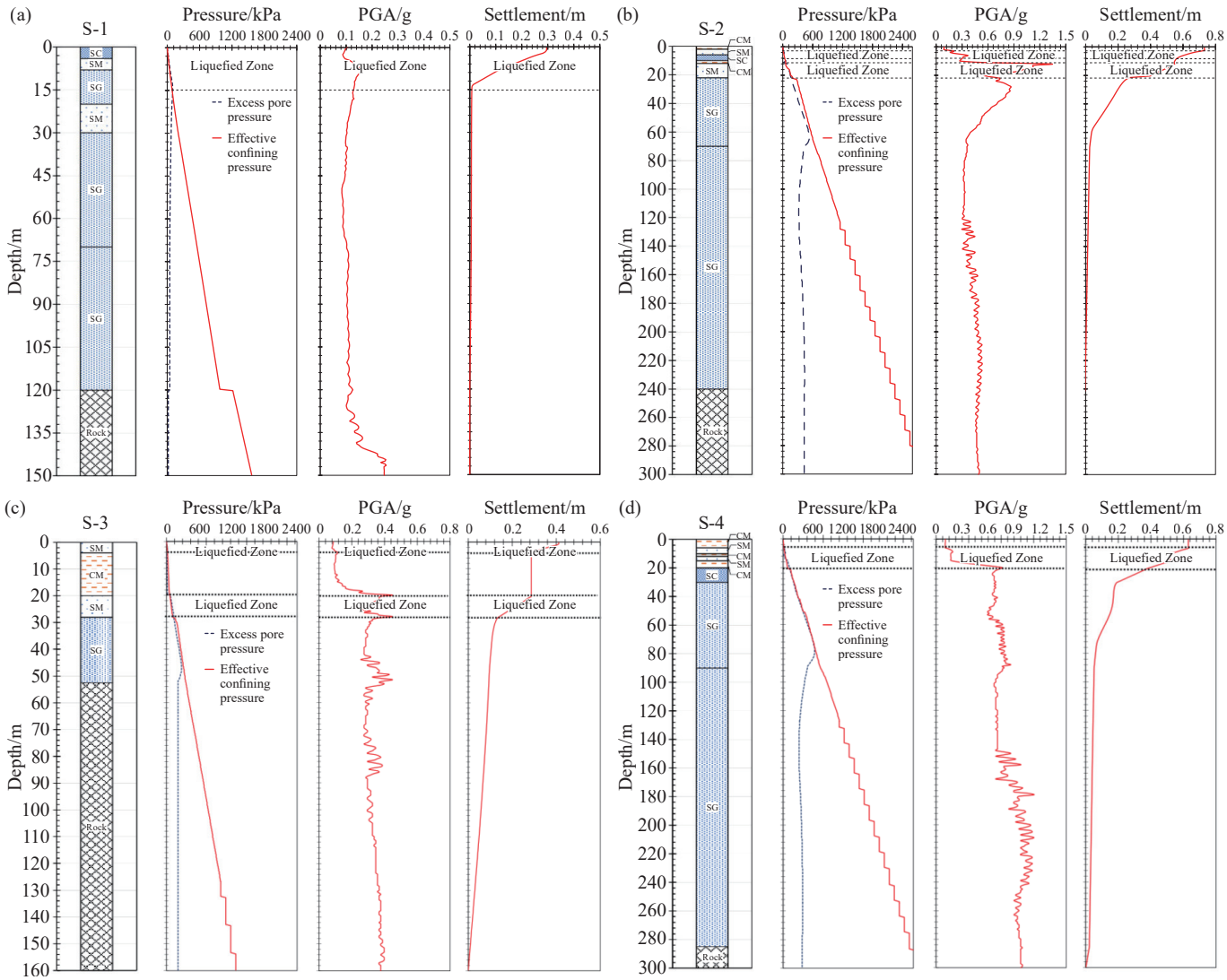

Fig. 11. Profiles of accelerations, pressures, and settlements during seismic wave propagation for a–S-1, b–S-2, c–S-3, and d–S-4.

surface is approximately 0.104g. For S-2 (Fig. 11b), the maximum acceleration at the ground surface during the earthquake is about 0.1g. However, a significant acceleration is noted as 1.33g at a depth of 12 m. For Fig. 11c (S-3), the maximum acceleration predicted at the ground surface is about 0.1g. At a depth of 20 m, the maximum acceleration could reach the value of 0.45g. At the ground surface in S-4 (Fig. 11d), the acceleration decreases to 0.057g. However, in the liquefied layer, the maximum acceleration is about 0.408g.

Several studies define the liquefaction threshold as a PGA of 0.09g (Kramer SL and Stewart JP, 1996; Santucci de Magistris F et al., 2013). This study's PGA of liquefied layers is generally more significant than the threshold. Deep-level sandy soils may liquefy if high amplitude ground motion is applied for an extended period, according to Huang Y and Yu M (2013). A larger PGA might be able to sustain the energy needed to build up pore pressure continuously. It makes sense then that liquefaction might occur at a lower depth.

3.3.3. Settlement profiles

For predicted settlement, during seismic wave propagation in S-1 (Fig. 11a), the settlement at the ground surface could be about 0.295 m. In contrast, in S-2 (Fig. 11b), the maximum settlement at the ground surface is about 0.732 m. For S-3 (Fig. 11c), The prediction of maximum settlement at the ground surface is about 0.411 m. For S-4 (Fig. 11d), the analysis shows that the maximum settlement at the ground surface is about 0.630 m. The massive excess pore pressure build-up could significantly raise the settlement due to the granular soil compaction during shaking. The uniform sandy soil deposits undergoing significant shaking during earthquakes could be why settlements occur. Several studies mentioned that the ground settlement followed by the massive flow-side during the 2018 Great Indonesia Earthquake could be caused by the excess pore pressure build-up and significant acceleration from earthquake shaking. Kiyota T et al. (2020) suggested that an upward dissipation of excess pore pressure and void redistribution occur in the liquefied soil, followed by ground settlement. In general, the combination of a thick sand layer and a significant peak ground acceleration confirms why the large settlement of the ground surface could happen during the earthquake.

3.4. Seismic Behaviour

This study exposes several liquefied depths for further discussion to observe the dynamic behaviour of soils under earthquake shaking. Figs. 12–15 present seismic behaviour for S-1 at a depth of 2 m, S-2 at a depth of 4 m, S-3 at a depth of 3 m, and S-4 at a depth of 8 m. Figs. 12a–15a show that peak ground acceleration in each representative depth observed varies from 0.091g to 0.164g. In line with the PGA for liquefaction threshold suggested by Santucci de Magistris F et al. (2013), it can be estimated that liquefaction may occur. Since the value of acceleration reached the threshold, it can be reasonable why liquefaction could occur. Figs. 12b–15b show that excess pore pressure build-up exceeds the initial effective stress. It is also a liquefaction indication observed in the representative layers. For an effective stress path, the effective stress path in Figs. 12c–15c showed that there is a significant reduction of effective stress due to excess pore pressure. The significant decrease in the effective stress path indicates that the soil mass loses bearing capacity and undergoes liquefaction. In Figs 12d–15d, the flattered curve of the hysteretic loop indicates that a non-linear response could occur during seismic wave propagation (Pender MJ et al., 2016). Shear strength is reduced when the shear modulus is reduced. Effective stress and shear strength are connected to the liquefaction phenomenon. As a result, decreasing the effective stress also lowers the shear modulus, which increases the possibility of liquefaction (Zhuang HY et al., 2018).

In Figs. 12e–15e, the spectral acceleration comparison is presented. For S-1 at a depth of 2 m (Fig. 12e), it can be observed that spectral acceleration is within the updated spectral acceleration. Additionally, Fig. 13e shows that the spectral acceleration in S-2 at a depth of 4 m is greater than the design spectral acceleration at a period of 2 s. It suggests that the impact of ground motion propagation may be considerable for high-story buildings. The comparison of spectral acceleration is done in Fig. 14e. The figure shows that, over an extended period, spectral acceleration at 4 m deep exceeds design spectral acceleration. Thus, the propagation of seismic waves may significantly affect tall buildings. The comparison of spectral acceleration is also shown in Fig. 15e. The spectral acceleration from the seismic ground response analysis can be seen to exceed the design spectral acceleration over an extended period, much like other previously studied sites.

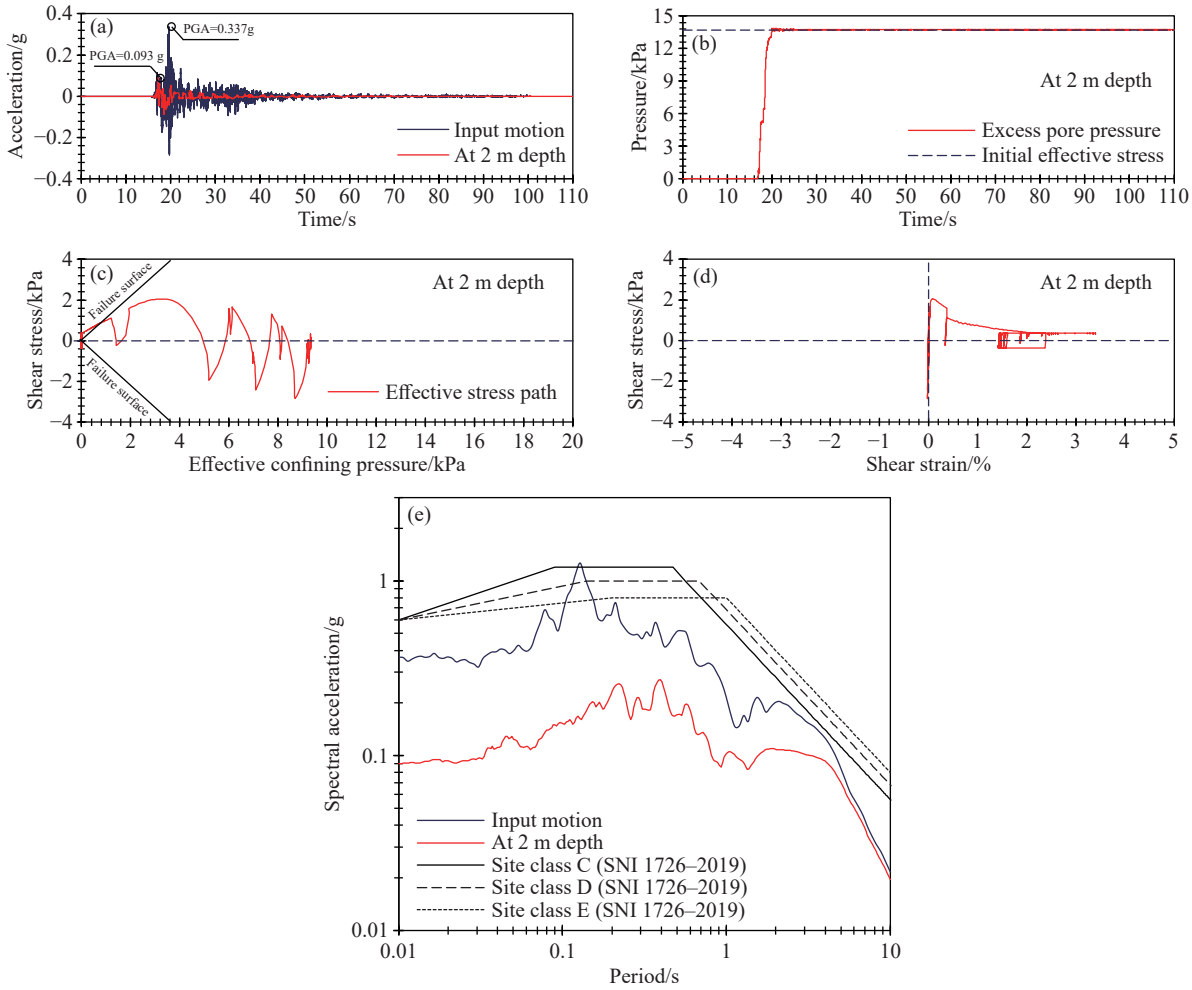

Fig. 12. Dynamic behaviour at a depth of 2 m in S-1. a–Time-history acceleration; b–excess pore pressure; c–effective stress path; d–hysteretic loop; e–spectral acceleration.

3.5. Significant liquefaction duration

This study predicts significant liquefaction duration (SD_{Liq}) based on Arias Intensity (AI). AI and energy flux can be generated from the ground motion in the liquefied layer. Based on those two variables, (SD_{Liq}) can be estimated. The prediction is based on the initial time of liquefaction and the end time of liquefaction. The Arias intensity in the liquefiable layer is also presented. Prediction of Arias Intensity at the initial time of liquefaction and the end time of liquefaction are estimated. From both arias intensity and time, significant liquefaction duration (SD_{Liq}) is predicted by calculating the gap.

Fig. 16 shows that for the depth on each investigated site, the initial liquefaction time generally occurs from 14.26 s to 19.93 s. Liquefaction in each investigated depth generally stops at the observed time, varying from 31.97 s to 100 s. Therefore, the liquefaction duration in the representative depth in each investigated site is observed to vary from 15.19 s to 81.69 s. In the depth of the sites under investigation, the minimum AI required to initiate liquefaction ranges from 25.767% to 72.952%, while the maximum AI required to do so is observed to range from 93.246% to 100%. Based on the analysis, it is estimated that S-4 has the shortest liquefaction duration at a depth of 8 m. The longest liquefaction duration is recorded in S-3 at a depth of 2 m. As stated differently, shallow sandy soils may experience the longest duration and vice versa.

Fig. 17 presents the correlation between AI values during liquefaction for representative sites and energy flux. AI values are crucial in understanding the energy flux required to trigger liquefaction. The figure shows that the AI required to trigger initial liquefaction is about 25% to 73%, and the AI required for final liquefaction is about 93% to 100% for the representative liquefaction depth. These values indicate the energy flux required for triggering liquefaction, which is about 902 cm^2/s to 1419 cm^2/s, and for final liquefaction, timing is about 2,083 cm^2/s to 199,853 cm^2/s. The analysis shows that the energy flux for a deeper liquefiable layer tends to be smaller than a shallow liquefiable layer. The results also show that the liquefaction duration for a shallow liquefiable depth tends to be longer than a deeper one, as presented in Fig. 18.

3.6. Liquefaction damage, hazard assessment, and countermeasure effort

The analysis results show that liquefaction during the

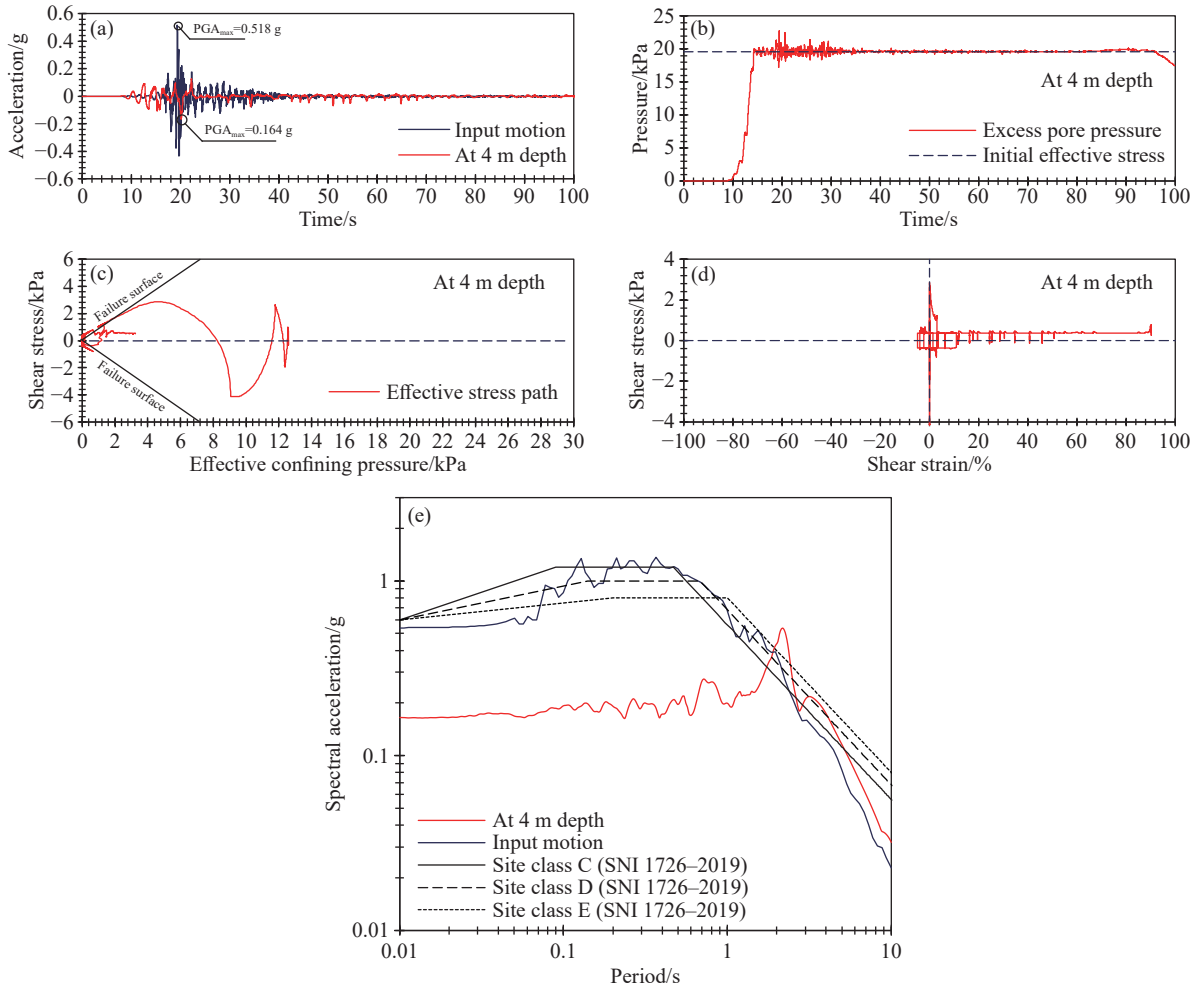

Fig. 13. Dynamic behaviour at a depth of 4 m in S-2. a–Time-history acceleration; b–excess pore pressure; c–effective stress path; d–hysteretic loop; e–spectral acceleration.

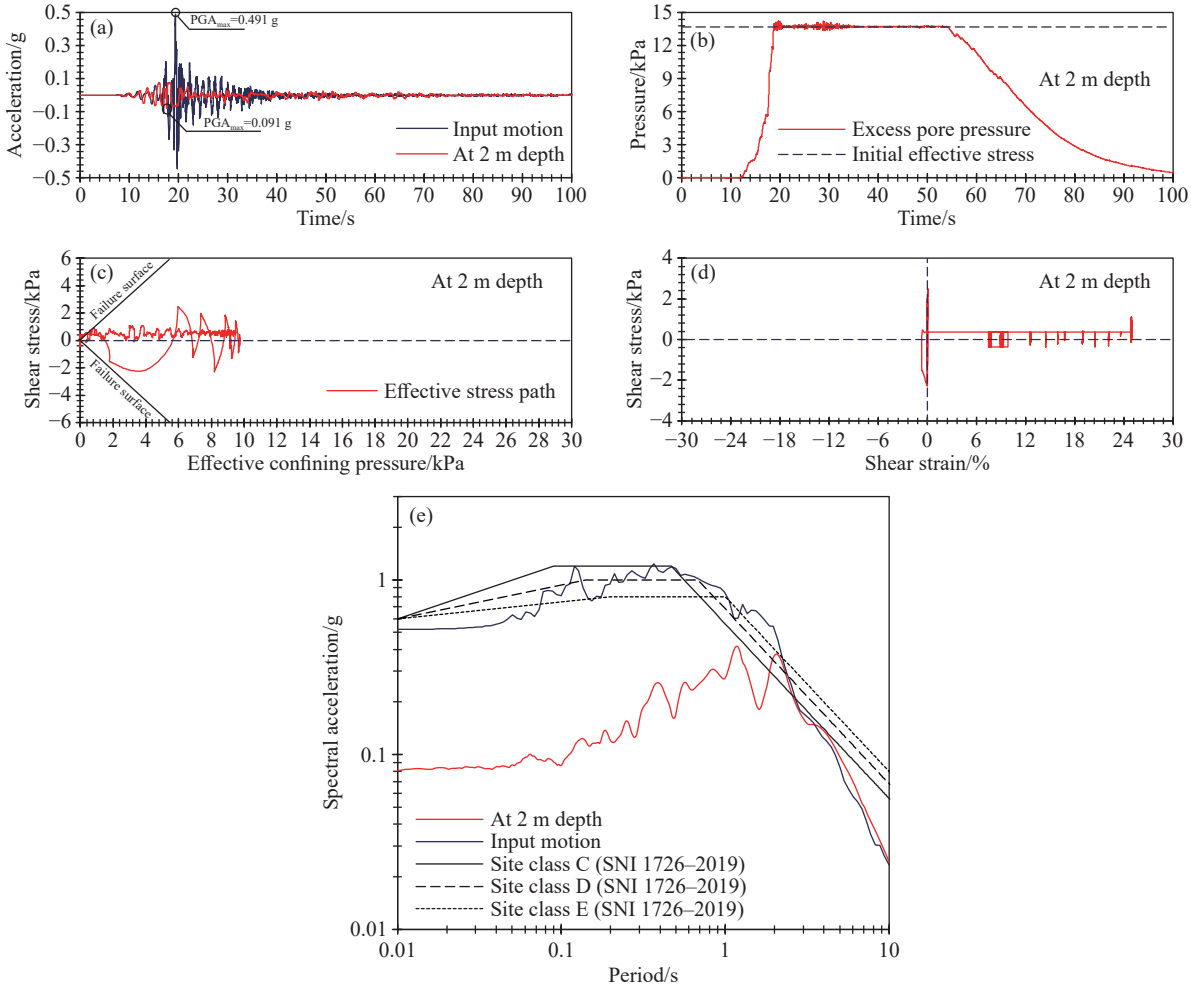

Fig. 14. Dynamic behaviour at a depth of 2 m in S-3. a–Time-history acceleration; b–excess pore pressure; c–effective stress path; d–hysteretic loop; e–spectral acceleration.

2018 Great Indonesia Earthquake in Palu was highly significant. The combination of strong ground motion and extended duration triggered deep and extensive liquefaction in the study area. Several previous studies have confirmed that liquefaction caused various types of damage. Triyono R et al. (2024) reported that deep cyclic mobility liquefaction in Palu occurred during the mainshock and subsequent aftershocks within 25 minutes. They also suggested that geological structure, groundwater level, and earthquake risk play essential roles in triggering liquefaction.

Multiple studies, including those by Kusumawardani R et al. (2021), Zhao B (2021) and Tanjung MI et al. (2023), have emphasized that the earthquake led to flow liquefaction, particularly in hilly areas with gentle slopes. Bradley K et al. (2019) stressed that the 2018 liquefaction in Palu and its devastating impacts could have been avoided if not for a raised water table, especially on hilly slopes. Neglecting the earthquake-triggered landsliding of gentle, irrigated alluvial slopes poses a significant hazard. The dense settlements in hilly to plain areas in Palu heighten the risk of liquefaction. Urgent attention is needed to address the shallow groundwater, which contributes to a higher liquefaction potential. Consequently, the impacted area is primarily characterized by loose and saturated alluvial-sedimented materials.

The liquefaction in Palu highlights the critical importance of hazard assessment before construction. Understanding geological characteristics and the risk of liquefaction during an earthquake should be thoroughly achieved. Additionally, site investigations to obtain soil characteristics should be enforced. These investigations can provide general information on liquefaction potential, which can inform land-use policy recommendations. Engineers can refer to the liquefaction hazard map when determining suitable foundations. Spatial development based on seismic hazard mitigation, especially liquefaction, should be prioritised.

In line with the liquefaction potential analysis, the countermeasure to reduce the liquefaction potential should be performed to anticipate severe damage if a large earthquake occurs. In line with this condition, Gómez-Martínez F et al. (2020) suggested that the enforcement of foundation design considering the potential impact of liquefaction should be addressed. Brevik and Miller EC (2015) and Vessia G et al. (2021) stated that a detailed geological study should improve soil resistance for areas with high seismic impact potential. In addition, liquefaction would lead to significant damage in

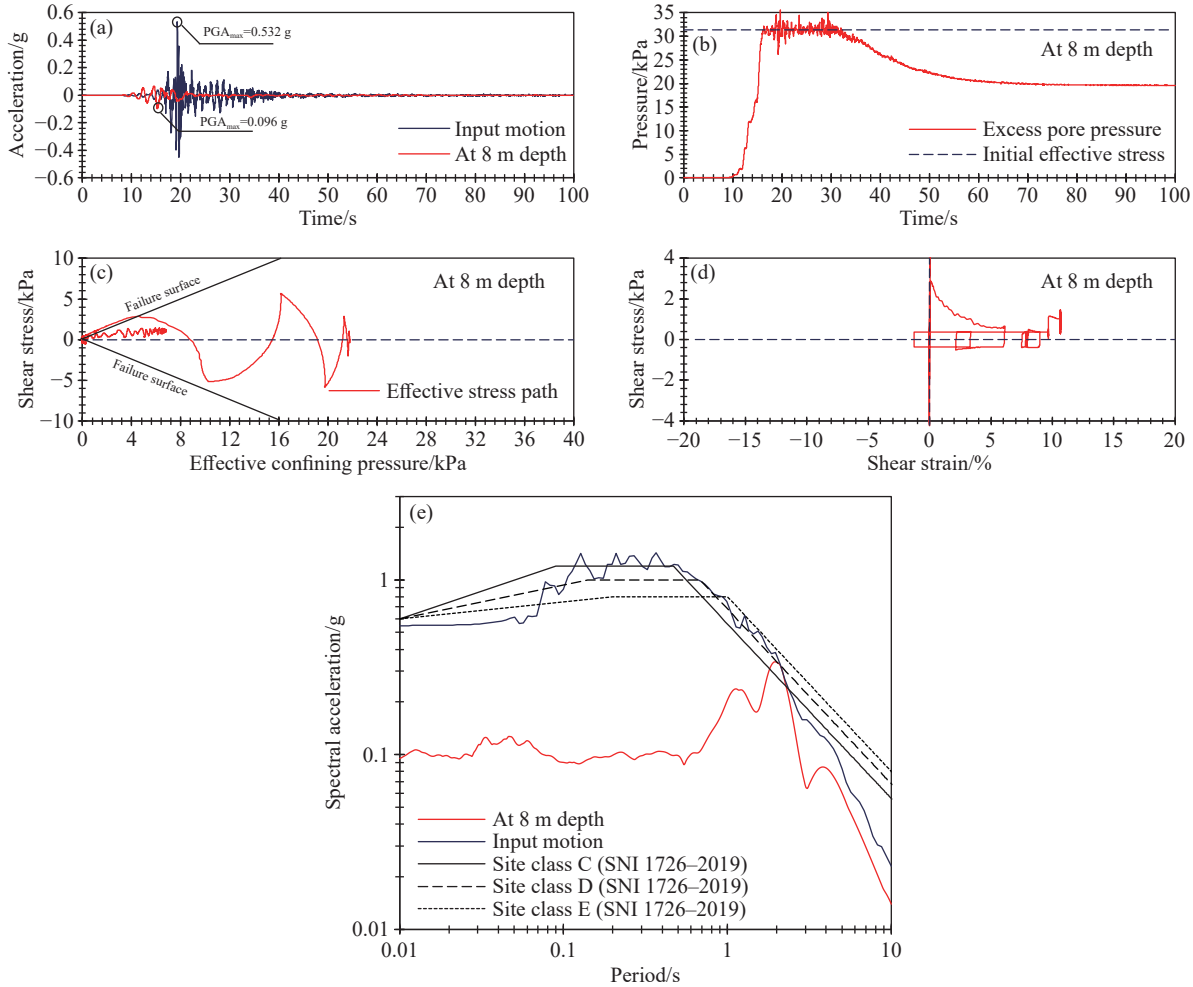

Fig. 15. Dynamic behaviour at depth of 8 m in S-4. a–Time-history acceleration; b–excess pore pressure; c–effective stress path; d–hysteretic loop; e–spectral acceleration.

areas dominated by loose sandy soils, mainly if the areas are generally centralised for infrastructures and housing. Spatial development based on seismic hazard and integrated liquefaction assessments can be first performed (Mase LZ, 2024). In general, information on liquefaction susceptibility is essential for countermeasure action. Several methods, such as geotextile infiltration (Indhanu T et al., 2023), partial saturation (Seyedi-Viand SM and Eseller-Bayat EE, 2022), drainage (Farzalizadeh R et al., 2021) and wasting materials innovation (Hazarika H et al., 2021) could be alternatives to mitigate liquefaction.

4. Conclusions

Several conclusions can be drawn in the following,

(i) Seismic ground motion, which refers to the movement of the ground during an earthquake, significantly contributes to the earthquake's impact. Ground motion in the vertical direction (UD) significantly affects and damages the study area. This vertical ground motion can lead to soil liquefaction, where soil loses its strength and behaves like a liquid, causing significant damage to structures and infrastructure.

(ii) The contribution of a significant peak ground acceleration and the geological condition of the study area could trigger liquefaction significantly. The potential impact of liquefaction, particularly near the ground surface, should be a cause for concern, as it could lead to a sudden massive displacement during an earthquake.

(iii) Based on the analysis, deep liquefaction could occur during the earthquake. To minimise the impact, liquefaction countermeasures should be implemented. This proactive planning is crucial, and the government should enforce the importance of site investigation to learn the geological characteristics and potential seismic damage in the study area.

(iv) This study found a connection between energy flux, AI, and the significant duration of liquefaction (SD_{Liq}). A longer liquefaction duration tends to happen for sandy layers on the ground surface and vice versa. This study found that a smaller gap of AI for liquefaction time indicates a short duration of liquefaction. A short duration means a smaller gap of energy flux released for liquefaction.

(v) An experimental test should be performed to investigate liquefaction resistances and parameters. The liquefaction resistance could be justified in the analysis to determine liquefaction parameters for better data for the experimental tests that would produce better results in analysis. The experimental test to obtain detailed

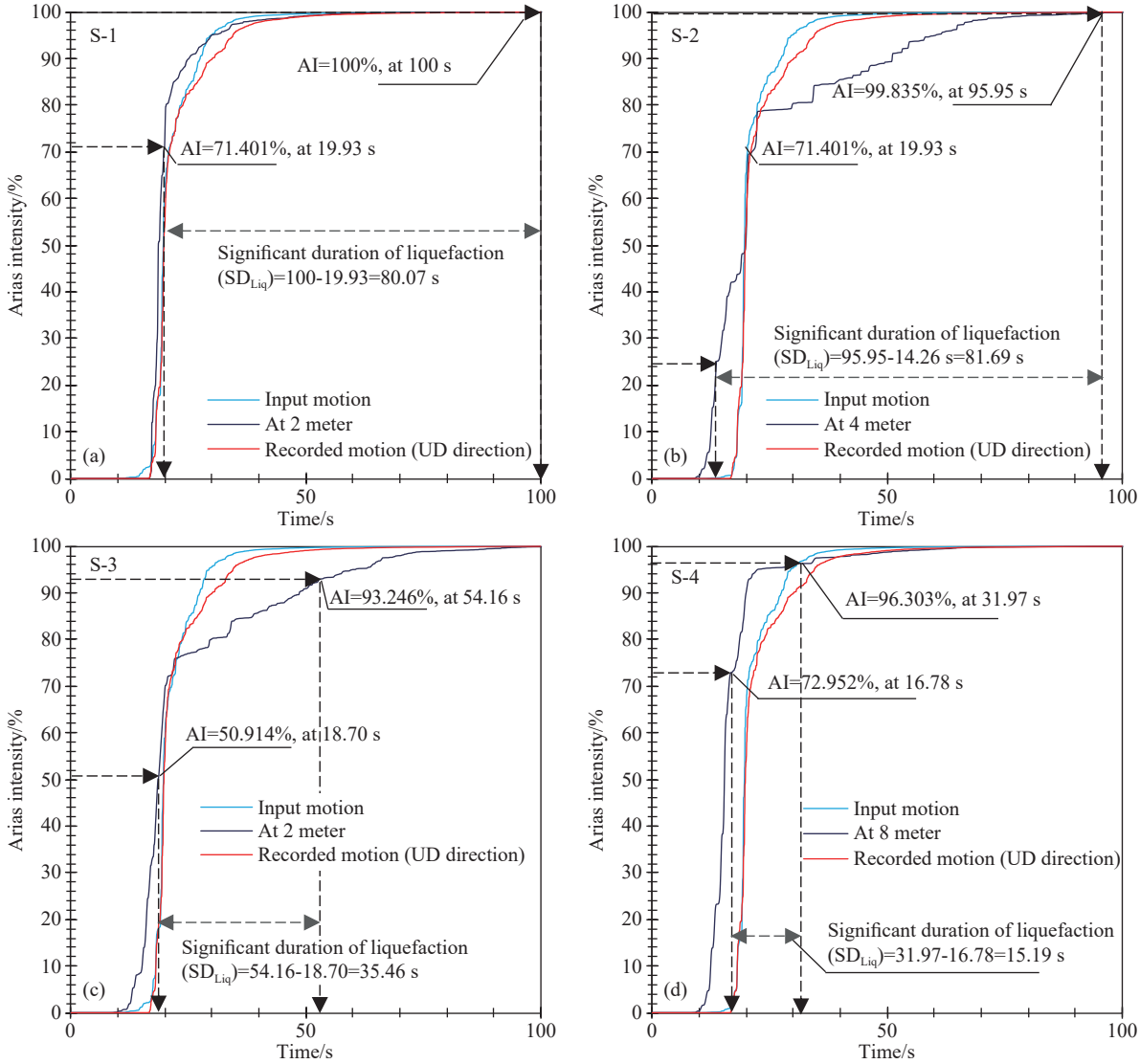

Fig. 16. Identification of significant duration based on Arias Intensity (I). a–S-1 at depth of 2 m; b–S-2 at a depth of 4 m; c–S-3 at a depth of 2 m; d–S-4 at a depth of 8 m.

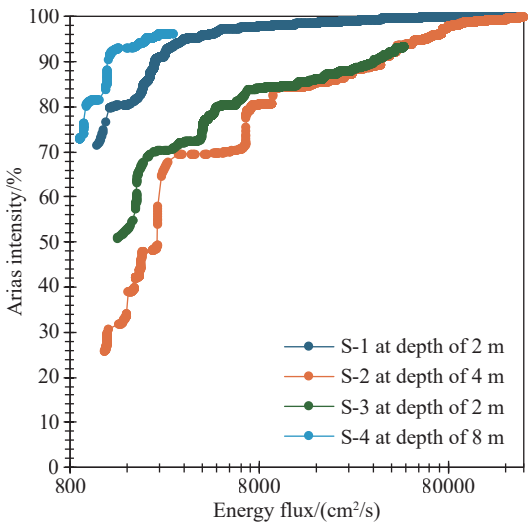

Fig. 17. Correlation between energy flux and Arias Intensity for representative liquefiable depths in the investigated sites.

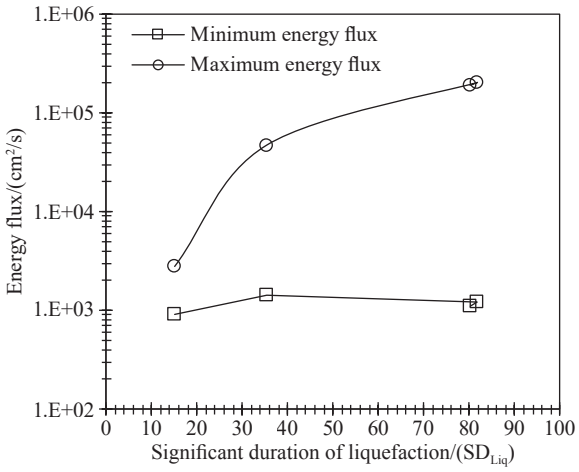

Fig. 18. Comparison between energy flux and significant duration of liquefaction for representative liquefiable depths in the investigated.

characteristics of liquefaction resistance can be obtained. It will be presented in further studies.

CRediT authorship contribution statement

Lindung Zalbuin Mase: Conceptualization, Software, Validation, Formal analysis, Investigation, Resources, Writing - Original Draft, Project administration. Weeradetch Tanapalungkorn: Data Curation, Visualization. Suched Likitlersuang: Methodology, Writing-Review & Editing, Supervision. Kyohei Ueda: Writing-Review & Editing, Funding acquisition. Tetsuo Tobita: Supervision, Funding acquisition.

Declaration of competing interest

The authors declare no conflicts of interest.

Acknowledgements

The World Class Professor (WCP) Program of the Directorate of Resources, Directorate General of Higher Education, Ministry of Education and Culture in 2023 supports this study. This study is being conducted under the JAPAN-ASEAN Science and Technology Innovation Platform (JASTIP-WP4). The first author (LZ Mase) acknowledges the University of Bengkulu's International Collaboration Research Fund (2183/UN30.15/LT/2019) for partial funding. The second author (W. Tanapalungkorn) acknowledges the C2F Fund for Postdoctoral Fellowship from Chulalongkorn University. The third author (S. Likitlersuang) acknowledges the Thailand Science Research and Innovation Fund Chulalongkorn University (DISF68210001) and the National Research Council of Thailand (N42A670572). The authors also appreciate the Agency of Meteorology, Climatology, and Geophysics in Indonesia for providing the study's supporting data.

References

Abdulnaby W, Onur T, Gök R, Shakir AM, Mahdi H, Al-Shukri H, Numan NMS, Abd NA, Chlaib HK, Ameen TH, Ramthan A. 2020. Probabilistic seismic hazard assessment for Iraq. Journal of Seismology, 24(3), 595–611. doi: 10.1007/s10950-020-09919-2.

Abrahamson NA, Silva WJ, Kamai R. 2014. Summary of the ASK14 ground motion relation for active crustal regions. Earthquake Spectra, 30(3), 1025–1055. doi: 10.1193/070913eqs198m.

Atik LA. 2009. Spreadsheet of NGA-West 1 calculation. Pacific Earthquake Engineering Research Centre (PEER), CA, USA.

Atik LA, Youngs RR. 2014. Epistemic uncertainty for NGA-West2 models. Earthquake Spectra, 30(3), 1301–1318. doi: 10.1193/062813eqs173m.

Bellier O, Sébrier M, Beaudouin T, Villeneuve M, Braucher R, Bourlès D, Siame L, Putranto E, Pratomo I. 2001. High slip rate for a low seismicity along the Palu-Koro active fault in central Sulawesi (Indonesia). Terra Nova, 13(6), 463–470. doi: 10.1046/j.1365-3121.2001.00382.x.

Benjamin JR. 1988. A criterion for determining exceedance of the operating basis earthquake. EPRI report NP-5930. Electric Power Research Institute, Palo Alto, CA.

Boore DM, Stewart JP, Seyhan E, Atkinson GM. 2014. NGA-West2 equations for predicting PGA, PGV, and 5% damped PSA for shallow crustal earthquakes. Earthquake Spectra, 30(3), 1057–1085. doi: 10.1193/070113eqs184m.

Bradley K, Mallick R, Andikagumi H, Hubbard J, Meilianda E, Switzer A, Du NR, Brocard G, Alfian D, Benazir B, Feng GC, Yun SH, Majewski J, Wei SJ, Hill EM. 2019. Earthquake-triggered 2018 Palu valley landslides enabled by wet rice cultivation. Nature Geoscience, 12, 935–939. doi: 10.1038/s41561-019-0444-1.

Brevik EC, Miller BA. 2015. The use of soil surveys to aid in geologic mapping with an emphasis on the eastern and midwestern United States. Soil Horizons, 56(4), 1–9. DOI: 10.2136/sh15-01-0001

Cabañas L, Benito B, Herraiz M. 1997. An approach to the measurement of the potential structural damage of earthquake ground motions. Earthquake Engineering & Structural Dynamics, 26, 79–92. doi: 10.1002/(SICI)1096-9845(199701)26:1<79::AID-EQE624>3.0.CO;2-Y.

Campbell KW, Bozorgnia Y. 2014. NGA-West2 ground motion model for the average horizontal components of PGA, PGV, and 5% damped linear acceleration response spectra. Earthquake Spectra, 30(3), 1087–1115. doi: 10.1193/062913eqs175m.

Chiarelli AS, Shao JF, Hoteit N. 2003. Modeling of elastoplastic damage behavior of a claystone. International Journal of Plasticity, 19(1), 23–45. doi: 10.1016/S0749-6419(01)00017-1.

Chiou BS, Youngs RR. 2014. Update of the chiou and youngs NGA model for the average horizontal component of peak ground motion and response spectra. Earthquake Spectra, 30(3), 1117–1153. doi: 10.1193/072813EQS219M.

Cilia MG, Mooney WD, Nugroho C. 2021. Field insights and analysis of the 2018 Mw 7.5 Palu, Indonesia earthquake, tsunami and landslides. Pure and Applied Geophysics, 178(12), 4891–4920. doi: 10.1007/s00024-021-02852-6.

Cipta A, Robiana R, Griffin JD, Horspool N, Hidayati S, Cummins PR. 2017. A probabilistic seismic hazard assessment for Sulawesi, Indonesia. Geological Society, London, Special Publications, 441(1), 133–152. doi: 10.1144/sp441.6.

Cipta A, Rudyanto A, Afif H, Robiana R, Solikhin A, Omang A, Supartoyo, Hidayati S. 2021. Unearthing the buried Palu-Koro fault and the pattern of damage caused by the 2018 Sulawesi earthquake using HVSR inversion. Geological Society of London Special Publications, 501(1), 185–203. doi: 10.1144/SP501-2019-70.

Dafalias YF, Manzari MT, 1999. Modeling of fabric effect on the cyclic loading response of granular soils. In: Proceedings of ASCE 13th Engineering Mechanics Conference, 13–16 June, Baltimore, MD.

Dafalias YF, Popov EP. 1975. A model of nonlinearly hardening materials for complex loading. Acta Mechanica, 21(3), 173–192. doi: 10.1007/BF01181053.

Elgamal A, Yang Z, Lu J. 2006. Cyclic1D: A computer program for seismic ground response, Report No. SSRP-06/05. San Diego, La Jolla, CA, USA: Department of Structural Engineering, University of California. See http://soilquake.net/cyclic1d/index.html.

Faris F, Fathani TF, Wang FW. 2019. Report on the UNESCO chair workshop on geoenvironmental disaster reduction 28th April - 1st may, 2019, Palu - Jakarta, Indonesia. Geoenvironmental Disasters, 6(1), 12. doi: 10.1186/s40677-019-0129-5.

Farzalizadeh R, Hasheminezhad A, Bahadori H. 2021. Shaking table tests on wall-type gravel and rubber drains as a liquefaction countermeasure in silty sand. Geotextiles and Geomembranes, 49(6), 1483–1494. doi: 10.1016/j.geotexmem.2021.06.002.

Goda K, Mori N, Yasuda T, Prasetyo A, Muhammad A, Tsujio D. 2019. Cascading geological hazards and risks of the 2018 Sulawesi Indonesia earthquake and sensitivity analysis of tsunami inundation simulations. Frontiers in Earth Science, 7, 261. doi: 10.3389/feart.2019.00261.

Gómez-Martínez F, Millen MDL, Alves Costa P, Romão X. 2020. Estimation of the potential relevance of differential settlements in earthquake-induced liquefaction damage assessment. Engineering Structures, 211, 110232. doi: 10.1016/j.engstruct.2020.110232.

Gusman AR, Supendi P, Nugraha AD, Power W, Latief H, Sunendar H, Widiyantoro S, Daryono, Wiyono SH, Hakim A, Muhari A, Wang XM, Burbidge D, Palgunadi K, Hamling I, Daryono MR. 2019. Source model for the tsunami inside Palu bay following the 2018 Palu earthquake, Indonesia. Geophysical Research Letters, 46(15), 8721–8730. doi: 10.1029/2019gl082717.

Hall R. 2019. The subduction initiation stage of the Wilson cycle. Geological Society, London, Special Publications, 470(1), 415–437. doi: 10.1144/sp470.3.

Hancock J, Watson-Lamprey J, Abrahamson NA, Bommer* JJ, Markatis A, McCOYH E, Mendis R. 2006. An improved method of matching response spectra of recorded earthquake ground motion using wavelets. Journal of Earthquake Engineering, 10(sup001), 67–89. doi: 10.1080/13632460609350629.

Hashash YMA, Musgrove MI, Harmon JA, Groholski DR, Phillips CA, Park D. 2015. DEEPSOIL 6.1, user manual. Urbana: Board of Trustees of University of Illinois at Urbana Champaign.

Hazarika H, Pasha SMK, Ishibashi I, Yoshimoto N, Kinoshita T, Endo S, Karmokar AK, Hitosugi T. 2020. Tire-chip reinforced foundation as liquefaction countermeasure for residential buildings. Soils and Foundations, 60(2), 315–326. doi: 10.1016/j.sandf.2019.12.013.

Hazarika H, Rohit D, Pasha SMK, Maeda T, Masyhur I, Arsyad A, Nurdin S. 2021. Large distance flow-slide at Jono-Oge due to the 2018 Sulawesi earthquake, Indonesia. Soils and Foundations, 61(1), 239–255. doi: 10.1016/j.sandf.2020.10.007.

Hibsch C, Alvarado A, Yepes H, Perez VH, Sébrier M. 1997. Holocene liquefaction and soft-sediment deformation in Quito (Ecuador): A paleoseismic history recorded in lacustrine sediments. Journal of Geodynamics, 24(1–4), 259–280. doi: 10.1016/S0264-3707(97)00010-0.

Hollender F, Cornou C, Dechamp A, Oghalaei K, Renalier F, Maufroy E, Burnouf C, Thomassin S, Wathelet M, Bard PY, Boutin V, Desbordes C, Douste-Bacqué I, Foundotos L, Guyonnet-Benaize C, Perron V, Régnier J, Roullé A, Langlais M, Sicilia D. 2018. Characterization of site conditions (soil class, VS30, velocity profiles) for 33 stations from the French permanent accelerometric network (RAP) using surface-wave methods. Bulletin of Earthquake Engineering, 16(6), 2337–2365. doi: 10.1007/s10518-017-0135-5.

Holzer TL, Bennett MJ, Ponti DJ, Tinsley JC. 1999. Liquefaction and soil failure during 1994 northridge earthquake. Journal of Geotechnical and Geoenvironmental Engineering, 125(6), 438–452. doi: 10.1061/(asce)1090-0241(1999)125:6(438).

Huang C, Galasso C. 2019. A comparison of NGA-West2 ground-motion models to recent Chinese data. Soil Dynamics and Earthquake Engineering, 125, 105677. doi: 10.1016/j.soildyn.2019.05.016.

Huang Y, Yu M. 2013. Review of soil liquefaction characteristics during major earthquakes of the twenty-first century. Natural Hazards, 65(3), 2375–2384. doi: 10.1007/s11069-012-0433-9.

Idriss IM. 2014. An NGA-West2 empirical model for estimating the horizontal spectral values generated by shallow crustal earthquakes. Earthquake Spectra, 30(3), 1155–1177. doi: 10.1193/070613EQS195M.

Indhanu T, Srisakul W, Chompoorat T, Chub-uppakarn T. 2023. Evaluation and mitigation of ground loss and shear failure in silty sand due to static liquefaction potential with geotextile filtration. International Journal of Geosynthetics and Ground Engineering, 9(6), 80. doi: 10.1007/s40891-023-00496-1.

Irsyam M, Cummins PR, Asrurifak M, Faizal L, Natawidjaja DH, Widiyantoro S, Meilano I, Triyoso W, Rudiyanto A, Hidayati S, Ridwan M, Hanifa NR, Syahbana AJ. 2020. Development of the 2017 national seismic hazard maps of Indonesia. Earthquake Spectra, 36(1_suppl), 112–136. doi: 10.1177/8755293020951206.

Ishihara K, Tatsuoka F, Yasuda S. 1975. Undrained deformation and liquefaction of sand under cyclic stresses. Soils and Foundations, 15(1), 29–44. doi: 10.3208/sandf1972.15.29.

Jalil A, Fathani TF, Satyarno I, Wilopo W. 2021. Liquefaction in Palu: The cause of massive mudflows. Geoenvironmental Disasters, 8(1), 21. doi: 10.1186/s40677-021-00194-y.

Jaya A, Nishikawa O, Jumadil S. 2019. Distribution and morphology of the surface ruptures of the 2018 Donggala–Palu earthquake, Central Sulawesi, Indonesia. Earth, Planets and Space, 71(1), 144. doi: 10.1186/s40623-019-1126-3.

Katili JA. 1978. Past and present geotectonic position of Sulawesi, Indonesia. Tectonophysics, 45(4), 289–322. doi: 10.1016/0040-1951(78)90166-X.

Kiyota T, Furuichi H, Hidayat RF, Tada N, Nawir H. 2020. Overview of long-distance flow-slide caused by the 2018 Sulawesi earthquake, Indonesia. Soils and Foundations, 60(3), 722–735. doi: 10.1016/j.sandf.2020.03.015.

Komura K, Sugimoto J. 2021. Shortcut faults and lateral spreading activated in a pull-apart basin by the 2018 Palu earthquake, central Sulawesi, Indonesia. Remote Sensing, 13(15), 2939. doi: 10.3390/rs13152939.

Kramer SL, Stewart JP. 1996. Geotechnical earthquake engineering. 2nd Ed. Boca Raton: CRC Press, 2024. doi: 10.1201/9781003512011.

Kusumawardani R, Chang M, Upomo TC, Huang RC, Fansuri MH, Prayitno GA. 2021. Understanding of Petobo liquefaction flowslide by 2018. 09. 28 Palu-Donggala Indonesia earthquake based on site reconnaissance. Landslides, 18(9), 3163–3182. doi: 10.1007/s10346-021-01700-x.

Lee SJ, Wong TP, Lin TC, Liu TY. 2019. Complex triggering supershear rupture of the 2018 Mw 7.5 Palu, Indonesia, earthquake determined from teleseismic source inversion. Seismological Research Letters, 90(6), 2111–2120. doi: 10.1785/0220190111.

Liu C, Shi YL. 2021. Space-time stress variations on the Palu-Koro fault impacting the 2018 Mw 7.5 Palu earthquake and its seismic hazards. Geochemistry, Geophysics, Geosystems, 22(5), e2020GC009552. doi: 10.1029/2020gc009552.

Mase LZ. 2017. Liquefaction potential analysis along coastal area of Bengkulu province due to the 2007 Mw 8. 6 Bengkulu earthquake. Journal of Engineering and Technological Sciences, 49(6), 721–736. doi: 10.5614/j.eng.technol.sci.2017.49.6.2.

Mase LZ, Likitlersuang S, Tobita T. 2019. Cyclic behaviour and liquefaction resistance of Izumio sands in Osaka, Japan. Marine Georesources & Geotechnology, 37(7), 765–774. doi: 10.1080/1064119x.2018.1485793.

Mase LZ, Likitlersuang S. 2021. Implementation of seismic ground response analysis in estimating liquefaction potential in northern Thailand. Indonesian Journal on Geoscience, 8(3), 371–383. doi: 10.17014/ijog.8.3.371-383.

Mase LZ, Fathani TF, Adi AD. 2021a. A simple shaking table test to measure liquefaction potential of Prambanan area, Yogyakarta, Indonesia. ASEAN Engineering Journal, 11(3), 89–108. doi: 10.11113/aej.v11.16874.

Mase LZ, Likitlersuang S, Tobita T. 2021b. Ground motion parameters and resonance effect during strong earthquake in northern Thailand. Geotechnical and Geological Engineering, 39(3), 2207–2219. doi: 10.1007/s10706-020-01619-5.

Mase LZ, Tanapalungkorn W, Likitlersuang S, Ueda K, Tobita T. 2022a. Liquefaction analysis of Izumio sands under variation of ground motions during strong earthquake in Osaka, Japan. Soils and Foundations, 62(5), 101218. doi: 10.1016/j.sandf.2022.101218.

Mase LZ, Likitlersuang S, Tobita T. 2022b. Verification of liquefaction

potential during the strong earthquake at the border of Thailand-Myanmar. Journal of Earthquake Engineering, 26(4), 2023–2050. doi: 10.1080/13632469.2020.1751346.

Mase LZ. 2024. Cumulative liquefaction susceptibility index to estimate integrated liquefaction at Bengkulu city, Indonesia. Transportation Infrastructure Geotechnology, 11(5), 3496–3529. doi: 10.1007/s40515-024-00417-3.

Mase LZ, Agustina S, Hardiansyah, Farid M, Supriani F, Tanapalungkorn W, Likitlersuang S. 2023. Application of simplified energy concept for liquefaction prediction in Bengkulu city, Indonesia. Geotechnical and Geological Engineering, 41(3), 1999–2021. doi: 10.1007/s10706-023-02388-7.

Meltzner AJ, Sieh K, Abrams M, Agnew DC, Hudnut KW, Avouac JP, Natawidjaja DH. 2006. Uplift and subsidence associated with the great Aceh-Andaman earthquake of 2004. Journal of Geophysical Research: Solid Earth, 111(B2), 2005JB003891. doi: 10.1029/2005jb003891.

Miller RD, Xia JH, Park CB, Ivanov JM. 1999. Multichannel analysis of surface waves to map bedrock. The Leading Edge, 18(12), 1392–1396. doi: 10.1190/1.1438226.

Mróz Z. 1967. On the description of anisotropic workhardening. Journal of the Mechanics and Physics of Solids, 15(3), 163–175. doi: 10.1016/0022-5096(67)90030-0.

Munson PJ, Ann Munson C, Pond EC. 1995. Paleoliquefaction evidence for a strong holocene earthquake in south-central Indiana. Geology, 23(4), 325. doi: 10.1130/0091-7613(1995)023<0325:pefash>2.3.co;2.

Natawidjaja DH, Daryono MR, Prasetya G, Udrekh, Liu PL, Hananto ND, Kongko W, Triyoso W, Puji AR, Meilano I, Gunawan E, Supendi P, Pamumpuni A, Irsyam M, Faizal L, Hidayati S, Sapiie B, Kusuma MA, Tawil S. 2021. The 2018 Mw7.5 Palu 'supershear' earthquake ruptures geological fault's multisegment separated by large bends: results from integrating field measurements, LiDAR, swath bathymetry and seismic-reflection data. Geophysical Journal International, 224(2), 985–1002. doi: 10.1093/gji/ggaa498.

National Earthquake Hazard Reduction Provision (NEHRP). 2015. Recommended Provisions for Seismic Regulation for New Buildings and Other Structures Edition, Part 1 – Provisions, Part 2 – Commentary. Report No. FEMA P-1050-1/2015 Federal Emergency Management Agency, USA.

Nemat-Nasser S, Tobita Y. 1982. Influence of fabric on liquefaction and densification potential of cohesionless sand. Mechanics of Materials, 1(1), 43–62. doi: 10.1016/0167-6636(82)90023-0.

Nemat-Nasser S, Zhang J. 2002. Constitutive relations for cohesionless frictional granular materials. International Journal of Plasticity, 18(4), 531–547. doi: 10.1016/s0749-6419(01)00008-0.

Nuttli OW. 1979. The relation of sustained maximum ground acceleration and velocity to earthquake intensity and magnitude. Miscellaneous Paper S-71-1, Report 16, U. S. Army Corps of Engineers, Waterways Experiment Station, Vicksburg, Mississippi, USA, 1979.

Okamura M, Ono K, Arsyad A, Minaka US, Nurdin S. 2020. Large-scale flowslide in Sibalaya caused by the 2018 Sulawesi earthquake. Soils and Foundations, 60(4), 1050–1063. doi: 10.1016/j.sandf.2020.03.016.

Park YJ, Ang AH, Wen YK. 1985. Seismic damage analysis of reinforced concrete buildings. Journal of Structural Engineering, 111(4), 740–757. doi: 10.1061/(asce)0733-9445(1985)111:4(740).

Parra-Colmenares EJ. 1996. Numerical modeling of liquefaction and lateral ground deformation including cyclic mobility and dilation response in soil systems. PhD Dissertation, Dept. Civil Engineering, Rensselaer Polytechnic Institute, New York.

Patria A, Putra PS. 2020. Development of the Palu–Koro fault in NW Palu Valley, Indonesia. Geoscience Letters, 7(1), 1–11. doi: 10.1186/s40562-020-0150-2

Pender MJ, Orense RP, Wotherspoon LM, Storie LB. 2016. Effect of permeability on the cyclic generation and dissipation of pore pressures in saturated gravel layers. Géotechnique, 66(4), 313–322. doi: 10.1680/jgeot.sip.15.p.024.

Prevost JH. 1985. A simple plasticity theory for frictional cohesionless soils. International Journal of Soil Dynamics and Earthquake Engineering, 4(1), 9–17. doi: 10.1016/0261-7277(85)90030-0.

Rusydi M, Efendi R, Sandra, Rahmawati. 2018. Earthquake hazard analysis use Vs30 data in Palu. Journal of Physics: Conference Series, 979, 012054. doi: 10.1088/1742-6596/979/1/012054.

Santucci de Magistris F, Lanzano G, Forte G, Fabbrocino G. 2013. A database for PGA threshold in liquefaction occurrence. Soil Dynamics and Earthquake Engineering, 54, 17–19. doi: 10.1016/j.soildyn.2013.07.011.

Sarma SK, Yang KS. 1987. An evaluation of strong motion records and a new parameter A_{95}. Earthquake Engineering & Structural Dynamics, 15(1), 119–132. doi: 10.1002/eqe.4290150109.

Scawthorn C. 2018. Earthquakes and their effects. The Engineering Handbook.

Seyedi-Viand SM, Eseller-Bayat EE. 2022. Partial saturation as a liquefaction countermeasure: A review. Geotechnical and Geological Engineering, 40(2), 499–530. doi: 10.1007/s10706-021-01926-5.

Seyhan E. 2014. Spreadsheet of NGA-West2 calculations. Pacific Earthquake Engineering Research Centre (PEER). CA, USA.

Simons W, Broerse T, Shen L, Kleptsova O, Nijholt N, Hooper A, Pietrzak J, Morishita Y, Naeije M, Lhermitte S, Herman M, Sarsito DA, Efendi J, Sofian, Govers R, Vigny C, Abidin HZ, Pramono GH, Nugroho C, Visser P, Riva R. 2022. A tsunami generated by a strike-slip event: Constraints from GPS and SAR data on the 2018 Palu earthquake. Journal of Geophysical Research: Solid Earth, 127(12), e2022JB024191. doi: 10.1029/2022jb024191.

SNI 1726-1019. 2019. Structural concrete requirements for buildings. National Standardization Agency, Jakarta, Indonesia.

Socquet A, Simons W, Vigny C, Mccaffrey R, Subarya C, Sarsito D, Ambrosius B, Spakman W. 2006. Microblock rotations and fault coupling in SE Asia triple junction (Sulawesi, Indonesia) from GPS and earthquake slip vector data. Journal of Geophysical Research: Solid Earth, 111, B08409. doi: 10.1029/2005JB003963.

Socquet A, Hollingsworth J, Pathier E, Bouchon M. 2019. Evidence of supershear during the 2018 magnitude 7. 5 Palu earthquake from space geodesy. Nature Geoscience, 12, 192–199. doi: 10.1038/s41561-018-0296-0.

Somantri AK, Mase LZ, Susanto A, Gunadi R, Febriansya A. 2023. Analysis of ground response of bandung region subsoils due to predicted earthquake triggered by lembang fault, west Java Province, Indonesia. Geotechnical and Geological Engineering, 41(2), 1155–1181. doi: 10.1007/s10706-022-02328-x.

Tanapalungkorn W, Mase LZ, Latcharote P, Likitlersuang S. 2020. Verification of attenuation models based on strong ground motion data in northern Thailand. Soil Dynamics and Earthquake Engineering, 133, 106145. doi: 10.1016/j.soildyn.2020.106145.

Tanjung MI, Irsyam M, Sahadewa A, Iai S, Tobita T, Nawir H. 2022. Flowslide due to liquefaction in Petobo during the 2018 Palu earthquake. Proceedings of the 4th International Conference on Performance Based Design in Earthquake Geotechnical Engineering (Beijing 2022). Cham: Springer International Publishing, 565–579. doi: 10.1007/978-3-031-11898-2_33.

Tanjung MI, Irsyam M, Sahadewa A, Iai S, Tobita T, Nawir H. 2023. Overview of flowslide in Petobo during liquefaction of the 2018 Palu Earthquake. Soil Dynamics and Earthquake Engineering, 173, 108110. doi: 10.1016/j.soildyn.2023.108110.

Thein P, Pramumijoyo S, Brotopuspito K, Kiyono J, Wilopo W, Furukawa A, Setianto A. 2014. Estimation of seismic ground motion and shaking parameters based on microtremor measurements at Palu

city, central Sulawesi Province, Indonesia. World Academy of Science, Engineering and Technology, 8, 308–319.

Triyono R, Widiyantoro S, Zulfakriza Z, Supendi P, Rahman AS, Gunawan MT, Oktavia NH, Rahmatullah FS, Fadhilah FZ, Habibah NF, Sativa O, Permana D, Wallansha R, Octantyo AY, Persada YD, Pranata B, Sujabar S. 2024. Investigation of liquefaction in Balaroa, Petobo, and Jonooge (central Sulawesi, Indonesia) caused by the 2018 Palu earthquake sequence. Journal of Engineering and Technological Sciences, 56(3), 317–328. doi: 10.5614/j.eng.technol.sci.2024.56.3.1.

Ulrich T, Vater S, Madden EH, Behrens J, van Dinther Y, van Zelst I, Fielding EJ, Liang C, Gabriel AA. 2019. Coupled, physics-based modeling reveals earthquake displacements are critical to the 2018 Palu, Sulawesi tsunami. Pure and Applied Geophysics, 176(10), 4069–4109. doi: 10.1007/s00024-019-02290-5.

Vessia G, Laurenzano G, Pagliaroli A, Pilz M. 2021. Seismic site response estimation for microzonation studies promoting the resilience of urban centers. Engineering Geology, 284, 106031. doi: 10.1016/j.enggeo.2021.106031.

Von Thun JL, Roehm LH, Scott GA, Wilson JA. 1988. Earthquake ground motions for design and analysis of dams. Earthquake Engineering and Soil Dynamics II - Recent Advances in Ground-Motion Evaluation: Proceedings of the Specialty Conference, 463–481.

Walpersdorf A, Vigny C, Subarya C, Manurung P. 1998. Monitoring of the Palu-Koro fault (Sulawesi) by GPS. Geophysical Research Letters, 25(13), 2313–2316. doi: 10.1029/98gl01799.

Watkinson IM, Hall R. 2017. Fault systems of the eastern Indonesian triple junction: evaluation of quaternary activity and implications for seismic hazards. Geological Society, London, Special Publications, 441(1), 71–120. doi: 10.1144/sp441.8.

Widodo LE, Prassetyo SH, Simangunsong GM, Iskandar I. 2022. Role of the confined aquifer in the mechanism of soil liquefaction due to the 7. 5 Mw earthquake in Palu (Indonesia) on 28 September 2018. Hydrogeology Journal, 30(6), 1877–1898. doi: 10.1007/s10040-022-02516-2.

Wills CJ, Gutierrez CI, Perez FG, Branum DM. 2015. A next Generation V_{S30} Map for California based on geology and topography. Bulletin of the Seismological Society of America, 105(6), 3083–3091. doi: 10.1785/0120150105.

Wu DY, Ren ZK, Liu JR, Chen J, Guo P, Yin GM, Ran HL, Li CY, Yang XD. 2021. Coseismic surface rupture during the 2018 Mw 7.5 Palu earthquake, Sulawesi Island, Indonesia. GSA Bulletin, 133(5–6), 1157–1166. doi: 10.1130/B35597.1.

Yang Z, 2000. Numerical modeling of earthquake site response including dilation and Liquefaction. PhD Dissertation, Dept. of Civil Engineering and Engineering Mechanics, Columbia University, New York.

Yolsal-Çevikbilen S, Taymaz T. 2019. Source characteristics of the 28 September 2018 Mw 7.5 Palu-Sulawesi, Indonesia (SE Asia) earthquake based on inversion of teleseismic bodywaves. Pure and Applied Geophysics, 176(10), 4111–4126. doi: 10.1007/s00024-019-02294-1.

Yulianur A, Saidi T, Setiawan B, Sugianto S, Rusdi M. 2020. Microtremor measurement at liquefaction-induced ground deformation area. Journal of Engineering Science and Technology, 15(5), 2871–2889.

Zhuang HY, Wang R, Chen GX, Miao Y, Zhao K. 2018. Shear modulus reduction of saturated sand under large liquefaction-induced deformation in cyclic torsional shear tests. Engineering Geology, 240, 110–122. doi: 10.1016/j.enggeo.2018.04.018.

Zhao B. 2021. Landslides triggered by the 2018 Mw 7. 5 Palu supershear earthquake in Indonesia. Engineering Geology, 294, 106406. doi: 10.1016/j.enggeo.2021.106406.